Self-consistent atomic deformation method for application of density functional theory

L. L. Boyer

Department of Computational and Data Sciences, George Mason University, Fairfax, Virginia 22030, USA

H. T. Stokes

Department of Physics and Astronomy, Brigham Young University, Provo, Utah 84602, USA

M. M. Ossowski

Information Technology, Rice University, Houston, Texas 77251, USA

M. J. Mehl[*]

Center for Computational Materials Science, Naval Research Laboratory, Washington, DC 20375-5345, USA

We describe a computational method based on density functional theory in which the total electronic density is expressed as a sum over "atomic" densities or densities localized at atomic sites. The atomic densities are determined self-consistently from a variational treatment of the total energy, which includes terms to account for kinetic energy due to the overlapping densities from separate atomic sites. We call this method self-consistent atomic deformation. The self-consistent procedure involves formulation and calculation of a potential for each atomic site, solving a one-electron Schrödinger's equation for each site and using these self-consistent potentials and densities to compute total energy and forces. The associated numerical methods employed are described in detail and illustrated for selected examples.

I. INTRODUCTION

Following the development of the Thomas-Fermi-Dirac statistical method, the electronic density, rather than the wave function, often has been used as the basic variable for expressing the energy of a collection of atoms. In early applications of this density functional approach, the total density was simply assumed to be the sum of the densities of the separate atoms. This approach, discussed in chapter 1 of Born and Huang,[1] provided a qualitative description of atomic forces which guided the development of empirical models. A major advance was provided by Gordon and Kim[2] (GK) who obtained quantitative results for closed-shell systems by carefully evaluating "electron-gas" expressions using free-atom densities.

A few years before the GK work Hohenberg and Kohn[3] proved that the ground-state energy of a system of electrons was uniquely expressed as a functional of the density regardless of the external potential. This remarkable result added credibility to the density functional approach, although it evidently was not a motivating factor for the GK work. Soon after the Hohenberg-Kohn theorem was published Kohn and Sham[4] (KS) presented a variational method for applying the density functional approach to compute total energy from the Hohenberg-Kohn formalism. In this method the density of an N electron system is given by the sum of the squares of the N lowest-energy self-consistent solutions of an effective one-electron Schrödinger's equation whose potential is defined, variationally, to minimize the total energy. Ten years after the KS work and three years after that of GK, Janak *et al.*[5] computed total energies for nine elements with cubic structures, obtaining impressive results for cohesive energies, lattice constants, and bulk moduli. Several earlier total-energy calculations[6–10] achieved similar success on a smaller scale. The many calculations of total energy which followed this early work established the highly successful field known today as density functional theory (DFT).

In this paper, we describe a method for applying DFT, called self-consistent atomic deformation (SCAD), in which the electron density n is expressed as a sum over atomiclike densities n_i. Like the KS method, SCAD uses an assumed expression for total energy U as a functional of n, and n is determined from a variational treatment of $U[n]$. Both methods use the same approximate functional for exchange and correlation energy. Like the GK method, $U[n]$ includes a contribution to the kinetic energy from overlapping densities (T_k). SCAD requires that U be a minimum for small variations of each n_i. This provides an atomiclike Schrödinger equation to be solved for each atomic site with potentials that include contributions from the kinetic-energy overlap terms. Analogous to KS, the potentials are determined variationally from U.[11] The kinetic-energy overlap contributions to the potentials serve to localize the site densities with the size, shape, and total charge of each n_i determined by SCAD. The variational freedom in SCAD is contained in the one-electron atomiclike solutions of the Schrödinger equations for each atomic site. If $T_k = T_0$, the kinetic energy of noninteracting electrons, the expression for U becomes that of the KS formulation of DFT, for which adequate variational freedom comes from one-electron states that extend over the entire system, forming a band structure for crystals. Unlike the KS method, the SCAD method does not produce a band structure for crystals. However, if T_k is the "divine" functional,[12] i.e., T_0 for the KS method, or an unknown exact explicit functional of n, then both the KS and SCAD methods would give the same results for U and n. Thus, the

SCAD method could be helpful in testing approximations to the divine functional. The SCAD method may be considered to have some aspects of the KS method and orbital-free DFT methods.

The SCAD method can be viewed also as an extension of the GK model which allows complete relaxation of the atomic densities. This approach is taken also in the work of Cortona,[13,14] but with applications limited to densities expressed as overlapping spherical atoms. Other self-consistent atomic models can be found in the works of Muhlhausen and Gordon,[15] LaSar,[16] Bukowinski and co-workers,[17] and Edwardson.[18] Francisco *et al.*[19] included self-consistency in an atomic model that orthogonalizes the orbitals of an atom with those of its neighbors to obtain spherical densities and pair potentials following the GK method. The direct energy minimization technique of Lacks and Gordon,[20] which accounts for nonspherical ions by incorporating spherical bonding charges between spherical ions, has been quite successful in treating various oxides.

Our SCAD method evolved from an effort to extend the potential induced breathing model[21] to handle nonspherical ions, a feature known to be essential for treating oxide ferroelectrics.[22] Ivanov and Maksimov[23] developed a closely related approach to deal with nonspherical ions, including those in oxide ferroelectrics. We were motivated substantially by Edwardson's work together with a general effort to develop first-principles methods for ferroelectric materials.[24]

We have previously given brief discussions of the SCAD model,[11,25–28] which includes some applications of SCAD for spherically symmetric ions (SSCAD). A detailed description of the SSCAD method is given by Stokes *et al.*,[28] for which computer code is available. It has been applied in a cluster expansion technique to compute the MgO-CaO phase diagram.[29]

Our first application of SCAD for nonspherical atoms was to compute Born effective charges Z^*, the quantities that give the change in polarization produced by structural distortions, for ferroelectric oxides and alkaline-earth oxides.[30] The large values of Z^* for Ti, Nb, and certain oxygen ions in $BaTiO_3$ and $KNbO_3$ were shown to result primarily from large moments induced on the oxygen ions—a qualitative picture which agrees with subsequent calculations[31] using "maximally localized Wannier functions"[32] for associating portions of a KS derived charge density with particular atoms. Reasonable results for polarization and related properties have been obtained for a variety of compounds using the SCAD method.[33–37]

It has been argued[38] that the calculation of polarization using overlapping atomiclike densities, or Clausius-Mossotti-type models, is fundamentally flawed. However, the argument is based on a false assumption about the way polarization is computed in such models.[39] Specifically, the change in polarization that accompanies a structural distortion in a Clausius-Mossotti-type model is well defined provided the monopole charges are constant—that is, charge does not move from site to site, as expected for an insulator. Here we demonstrate how this picture follows from the SCAD formulation of DFT.

Previously proposed GK-type models rely on assumptions not related to approximations inherent in DFT to obtain site decomposed charge densities. The assumptions are then justified (or not) depending on the comparison of results with experiment. Unfortunately, it is not always clear if discrepancies result from the assumptions of the model or approximations inherent in the formulation of DFT. Prior to 2003 our applications of SCAD assumed that the radial components of basis functions used to treat free atoms were also adequate for treating overlapping atoms, and angular variations were limited to $l \leq 4$ in the spherical harmonics. Our first attempt to extend SCAD to larger l values was an application to the water molecule.[40] This provided a good, although limited, test—because SCAD treats the water molecule as an O^{--} ion in the presence of two protons. Thus, there is no overlap contribution to the kinetic energy, and SCAD becomes equivalent to the KS method. Recently, SCAD has been applied to AlF_3,[41] a compound that has a structural transition that provides a stringent test for DFT methods in general. These and additional results of SCAD calculations for AlF_3 are discussed below.

In this paper, we first give the formal description of the SCAD model. This is followed by details for calculating SCAD potentials, charge densities, total energies, and forces. Some of the details are expressed in Appendixes A–E. Then, the results are discussed for simple systems which illustrate how the kinetic-energy overlap potential prevents charge from flowing to neighboring sites. The section on charge densities includes a method for systematically improving the basis functions used to solve the Schrödinger equations to obtain results that depend only on the approximations used to formulate total energy. Next, we present results for AlF_3 which illustrate convergence issues, followed by a section with results for SiC and both make comparisons with KS and experimental results. Finally, we conclude with a discussion of some general features of the SCAD model which we have observed from applications on a variety of materials.

II. SCAD MODEL

Following Kohn and Sham[4] we write the total energy U as a functional of the electronic density n,

$$U[n(\mathbf{r})] = T[n(\mathbf{r})] + U_{es}[n(\mathbf{r})] + U_{xc}[n(\mathbf{r})], \qquad (1)$$

where T is the kinetic energy of noninteracting electrons at density n, U_{es} is the electrostatic energy, and U_{xc} is the exchange and correlation energy. We write the total density as a sum of atomiclike densities

$$n(\mathbf{r}) = \sum_i n_i(\mathbf{r} - \mathbf{R}_i) \qquad (2)$$

centered at $\mathbf{R}_i$, the location of nuclear charge Z_i. Each atomiclike density is expressed as a spherical harmonic expansion about an origin at its nucleus,

$$n_i(\mathbf{r}) = \sum_{l,m} n_{l,m}^{(i)}(r) Y_{l,m}(\hat{\mathbf{r}}). \qquad (3)$$

The ground state of the system will then be the set of n_i [or, alternatively, the $n_{l,m}^{(i)}$, which minimizes Eq. (1)], subject to the condition that the total number of electrons in the system is fixed.

To this point we have not made any approximation since the form of the charge density imposes no constraints. In other words, assuming we know the functionals in Eq. (1), the formulation for density is sufficiently general to determine the absolute minimum of U. Of course, we do not know T or U_{xc} exactly. In the SCAD method, the kinetic energy is approximated by

$$T[n(\mathbf{r})] = \sum_i T_0[n_i(\mathbf{r})] + T_k[n(\mathbf{r})] - \sum_i T_k[n_i(\mathbf{r})], \quad (4)$$

where $T_0[n_i(\mathbf{r})]$ is the kinetic energy of noninteracting electrons of density n_i in a potential v_i, centered at $\mathbf{R}_i$, and T_k is a functional to account for the noninteracting kinetic energy due to the overlapping of electronic densities from neighboring sites. If T_k is the exact kinetic energy for a noninteracting electron gas ($T_k = T_0$), then the first and third terms of Eq. (4) cancel. We assume the density associated with the ith site is given by $n_i = \sum_\alpha \psi^*_{\alpha,i} \psi_{\alpha,i}$, where $\psi_{\alpha,i}$ are solutions of a one-electron Schrödinger's equation with potential v_i. This provides a one to one correspondence between n_i and v_i. The necessary condition for U to be a minimum with respect to small variations of n_i leads to the following expression for v_i (Ref. 11):

$$v_i(\mathbf{r}) = v_{es}[n(\mathbf{r})] + v_{xc}[n(\mathbf{r})] + v_k[n(\mathbf{r})] - v_k[n_i(\mathbf{r})], \quad (5)$$

where v_{es} is the electrostatic potential due to the atomic nuclei and electron density, v_k is the functional derivative of T_k, and v_{xc} is the functional derivative of U_{xc} with respect to density. To compute n_i from v_i, we first express v_i in terms of spherical harmonics,

$$v_i(\mathbf{r}) = \sum_{l,m} v^{(i)}_{l,m}(r) Y_{l,m}(\hat{\mathbf{r}}), \quad (6)$$

and then solve the ith Schrödinger's equation. The details involved in these two steps are described in Secs. III A–III B.

The self-consistent solution for v_i (and hence, n_i and n), obtained by occupying the lowest one-electron energy levels for the entire system, allowing for charge transfer when indicated, minimizes the total energy in accord with Janak's theorem.[42] Of course, one is free to move charge from one atom to another in order to test the behavior of the energy as a function of charge transfer and demonstrate the satisfaction of Janak's theorem. See, for example, the results obtained using the SSCAD model,[28,30] SCAD results for the H_2O molecule,[40] and, in Sec VIA, SCAD results for crystalline SiC as a function of lattice parameter and charge transfer.

In principle, one could have a complete set of basis functions centered at site i with no basis functions, or less than complete sets of basis functions, centered on the other sites. Then the KS solution would result by formally putting all electrons on the ith site. T_k would not contribute because the rest of the sites would, formally, have only nuclear charge. In this case the outcome of SCAD would depend on the choice of assigning all charge to one atomic site. On the other hand, the question of uniqueness has not been a practical problem for SCAD in treating insulating systems with varying degrees of ionic bonding character, such as AlF_3 and SiC, discussed in detail below. For these types of systems, SCAD

determines the ions to have fully ionic (integer) monopole charges and accounts for bonding charge, normally associated with covalency, by distorting the negative-ion charge density. The uniqueness issue is further discussed in Sec IV using the example of a helium atom pair.

In this work we focus primarily on details of the SCAD method that are independent of the particular form of T_k and use the local Thomas-Fermi form for the overlap contribution to the noninteracting kinetic energy,

$$T_k = T_{TF} = A \int n^{5/3}(\mathbf{r}) d\mathbf{r}, \quad (7)$$

where

$$A = \frac{\pi^{4/3} 3^{5/3}}{10}. \quad (8)$$

(Hartree atomic units are used throughout this paper.) We have also derived potentials for generalized nonlocal functionals. For completeness and possible future use in the SCAD method, these results are included in Appendix A.

In its present form SCAD provides useful accuracy for many systems of interest and it is generally more efficient than KS calculations, particularly for large systems. The computational labor of SCAD increases approximately as $O(N)$ and the method is easily parallelized by assigning each processor computations for some fraction of N, the number of atoms in the system. Strictly speaking, our use of the Ewald method to include long-range interactions (Appendix C) takes $O(N^2)$ time, but this is not a significant factor for N less than a few hundred.

III. CALCULATION OF SCAD QUANTITIES

The procedure for obtaining a self-consistent solution for the total energy is easily stated. (1) Atomiclike densities are used to compute potentials at each site using Eq. (5). (2) New densities are obtained from the solutions of the corresponding one-electron Schrödinger's equations. Steps 1 and 2 are repeated, mixing new and old densities in each cycle, until convergence is achieved. In the final step, (3) the total energy and forces are determined from the converged potentials and densities. In practice, there are many details to be considered in each step. These are presented and discussed below in Secs. III A–III D (one each for energy and forces).

There are, of course, certain numerical techniques that are common to all three steps. For example, we represent both charge densities and potentials as sums over radial functions times spherical harmonics, a functional form that results naturally from the method we choose for solving the one-electron Schrödinger's equations. Presentation of details common to more than one section is done sequentially with appropriate references to the other sections and Appendixes A–E. Work to create computer code for the SCAD method began over ten years ago with separate codes developed independently at BYU and NRL. This parallel development strategy proved to be very useful for identifying the best algorithms and correcting errors. In Secs. III A–III D and the Appendixes A–E, SCAD is formulated in detail. For conve-

nience, we identify here a few symbols that are important for understanding the presentation of results in the remaining sections.

The set of basis functions at each atomic site are specified primarily by two symbols: (1) r_c, the radius of the maximum value of $r^2[r^l e^{-\alpha r^2}]^2$ for the smallest α in the set of basis functions of the form $r^l e^{-\alpha r^2} Y_{l,m}(\hat{\mathbf{r}})$, and (2) L, the maximum value of l in the set of spherical harmonic functions $Y_{l,m}(\hat{\mathbf{r}})$. Another quantity t specifies the amount of overlap between adjacent radial functions. Acceptable values for t lie in the range of $\sim 0.9 < t < \sim 0.8$. Values for L, r_c, and t, along with the atomic number, completely determine basis functions. Results are seen to converge abruptly with increasing r_c, showing localization of the SCAD atoms.

Another symbol R_c, not to be confused with r_c, is a cutoff radius beyond which interactions are included as point poles. In other words, the charge density of atoms or ions beyond R_c from atomic site i does not appreciably overlap with the ith atom. The value of R_c needs to be about two times the value of r_c for the largest atom or ion in the system.

A. Potential

In this section we address the following problem: Given the charge densities on each site i, expressed as in Eq. (3), determine similarly expressed potentials [Eq. (6)]. The radial dependencies of $n_{l,m}^{(i)}(r)$ and $v_{l,m}^{(i)}(r)$ and similar functions are kept on a mesh that starts at $r=0$ and has separations between points that increase logarithmically. A detailed discussion of the mesh and related integration, interpolation, etc., is offered in Appendix B.

First of all, we add and subtract the term $v_{xc}[n_i(\mathbf{r})]$ to the potential in Eq. (5),

$$v_i(\mathbf{r}) = v_{es}[n(\mathbf{r})] + v_{xc}[n_i(\mathbf{r})] + v_{ov}[n(\mathbf{r})] - v_{ov}[n_i(\mathbf{r})], \quad (9)$$

where $v_{ov} = v_k + v_{xc}$.

The electrostatic potential includes contributions from the nuclear charge as well as the electronic density and, unless the net moments of charge for $l \le 2$ happen to be zero, it is long ranged in nature; that is to say that contributions from all atoms in the system must be included. The electrostatic potential can be expressed as a linear superposition of the corresponding potentials of each "atom" or in any other way we want to partition the charge density. On the other hand, the overlap potential v_{ov} is a nonlinear function of the density and therefore cannot be so decomposed. Fortunately, it is short ranged and can be decomposed into a part that is smooth (compared to the behavior of the density in the vicinity of an atomic nucleus) and a part which, by design, is additive. The smooth part, along with other smooth parts, discussed below, and collectively called v_s, is computed on a three-dimensional grid with a relatively coarse radial mesh and a directional grid (over solid angle Ω) chosen for efficient integration (Appendix B).

Let R_c be a cutoff radius within which the densities of atom pairs have appreciable overlap. The potential due to atoms farther than R_c from the ith site are included using expressions for point poles. Contributions from monopoles, dipoles, and quadrupoles are computed using the Ewald

method while contributions from $l > 2$ poles are included in a similar manner with direct-space sums only (Appendix C). To account for the electrostatic potential due to near neighbors with separations $|\mathbf{R}_i - \mathbf{R}_j| < R_c$, one could "simply" transform the $Y_{l,m}$ expansions of $v_{es}^{(j)}$ to similar expansions about an origin at the ith site. The method for changing the origin of a spherical harmonic expansion (Löwdin transformation) is discussed in Appendix D. In fact, we include only the $l=0$ portion of the jth electrostatic potential using the Löwdin technique and include the $l > 0$ contributions, which are relatively smooth near the atomic nuclei, in v_s.

A smooth part of the overlap potential is created by adding and subtracting the term $\Sigma_j' v_{ov}[n_0^{(j)}(\mathbf{r})]$, where n_0 denotes the $l=0$ portion of the density and the prime on the summation indicates the $j=i$ term and terms with $|\mathbf{R}_i - \mathbf{R}_j| > R_c$ are omitted. The subtracted term combines with the last two terms of Eq. (9) to give the smooth overlap contribution included in v_s. The added term is included, along with the $l=0$ part of the electrostatic potential from near neighbors, using the Löwdin transformation.

The nonspherical part of the on-site exchange-correlation potential, defined by $v_{xc}[n_i(\mathbf{r})] - v_{xc}[n_0^{(i)}]$, is also smoothly varying, owing to the fact that the density becomes spherical near the nucleus. Therefore, it is conveniently included in v_s as well. The canceling term, $v_{xc}[n_0^{(i)}]$, is included as an on-site contribution. To summarize, the potential for the ith atom is decomposed, for computational purposes, as follows:

$$v_i(\mathbf{r}) = v_{on}^{(i)}(\mathbf{r}) + v_s^{(i)}(\mathbf{r}) + v_L^{(i)}(\mathbf{r}) + v_p^{(i)}(\mathbf{r}) + v_n^{(i)}(\mathbf{r}), \quad (10)$$

with subscripts denoting on-site, smooth, Löwdin, poles (outside R_c), and nuclear parts. The on-site nuclear part is included in v_{on} while nuclear contributions from far neighbors (outside R_c) are included in the monopole part of v_p. Thus, $v_n^{(i)}$ includes contributions from all nuclei contained in R_c except the one at site i.

The on-site term is the sum of the radial exchange-correlation term (introduced above to create a contribution to the smooth term) and the electrostatic potential due to the on-site electrons and the nuclear charge with atomic number Z_i.

$$v_{on}^{(i)}(\mathbf{r}) = v_{xc}[n_0^{(i)}(r)] + \int \frac{n_i(\mathbf{r}')}{|\mathbf{r} - \mathbf{r}'|} d\mathbf{r}' - \frac{Z_i}{r}, \quad (11)$$

where the second term is the Hartree potential $v_H(\mathbf{r})$. Substituting the expanded forms of n_i [Eq. (3)] and $|\mathbf{r} - \mathbf{r}'|^{-1}$ (addition theorem), the angular integrations are trivially performed to give

$$v_{on}^{(i;l,m)}(r) = \delta_{l0}\left(v_{xc}[n_0^{(i)}(r)] - \frac{\sqrt{4\pi}Z_i}{r} \right) + v_H^{(i;l,m)}(r). \quad (12)$$

where

$$v_H^{(i;l,m)}(r) = r^{-(l+1)} G_{l,m}^{(i)}(r) + r^l H_{l,m}^{(i)}(r), \quad (13)$$

$$G_{l,m}^{(i)}(r) = \frac{4\pi}{(2l+1)} \int_0^r x^{(l+2)} n_{l,m}^{(i)}(x) dx, \quad (14)$$

and

$$H_{l,m}^{(i)}(r) = \frac{4\pi}{(2l+1)} \int_r^\infty x^{(1-l)} n_{l,m}^{(i)}(x)\, dx. \tag{15}$$

The radial integrations are carried out as described in Appendix B. The values of $G_{l,m}^{(i)}(\infty)$ give the multipole moments that enter $v_p^{(i)}$ (see Appendix C).

The smooth potential

$$v_s^{(i)}(\mathbf{r}) = v_{xc}[n_i(\mathbf{r})] - v_{xc}[n_0^{(i)}(r)] + v_{ov}[n(\mathbf{r})] - v_{ov}[n_i(\mathbf{r})]$$
$$- \sum_j{}' v_{ov}[n_0^{(j)}(|\mathbf{r}-\mathbf{R}_j|)] + \sum_j{}' (v_H[n_j(\mathbf{r}-\mathbf{R}_j)]$$
$$- v_H[n_0^{(j)}(|\mathbf{r}-\mathbf{R}_j|)]) \tag{16}$$

is computed by accumulating values for the required densities and v_H on the coarse mesh centered at site i. This is the most time consuming part of the calculation. For every neighbor j the values of each radial function of the spherical harmonic expansions must be determined by interpolation and the corresponding values of $Y_{l,m}(\widehat{\mathbf{r}-\mathbf{R}_j})$ computed as well. Once values of $v_s^{(i)}(\mathbf{r})$ are determined on the coarse radial mesh, the coefficients of the spherical harmonic expansion are determined by numerical integration over solid angle Ω (Appendix B),

$$v_s^{(i;l,m)}(r) = \int v_s^{(i)}(\mathbf{r}) Y_{l,m}^*(\hat{\mathbf{r}})\, d\Omega. \tag{17}$$

The resultant functions of r are then interpolated from the coarse to the dense radial mesh.

The spherical harmonic expansion of the Löwdin potential

$$v_L^{(i)}(\mathbf{r}) = \sum_j{}' (v_{ov}[n_0^{(j)}(|\mathbf{r}-\mathbf{R}_j|)] + v_H[n_0^{(j)}(|\mathbf{r}-\mathbf{R}_j|)]) \tag{18}$$

is computed as described in Appendix D. Since it can have sharp features near the neighbors at $\mathbf{R}_j$, additional values are determined in these regions in order to accurately carry out integrations for contributions to the Hamiltonian matrix elements and total-energy. (See Appendix B).

Evaluation of the point-pole part of the potential (v_p) requires the multipole moments, i.e., the values of $G_{l,m}^{(i)}(\infty)$, combined with, for monopole terms, the nuclear charges (Z_i). Details of this part of the calculation are discussed in Appendix C.

Finally, we include the potential due to neighboring nuclei,

$$v_n^{(i)}(\mathbf{r}) = \sum_j{}' \frac{-Z_j}{|\mathbf{r}-\mathbf{R}_j|}, \tag{19}$$

where the sum over j excludes the $j=i$ term and terms with $|\mathbf{R}_i-\mathbf{R}_j| > R_c$. As already mentioned, contributions from nuclei outside the cutoff sphere are included in the monopole term of $v_p^{(i)}$ and the $i=j$ term is included in the on-site potential v_{on}. Spherical harmonic expansions about the ith site are given by the addition theorem. Another way to include v_n is to make it part of the Löwdin potential [Eq. (18)]. This was done to test the code. The amount of computations can be greatly reduced in many cases by making use of symmetry. Symmetry related details are discussed in Appendix E.

B. Charge density

To begin a SCAD calculation we need starting charge densities (n_i), to generate the first potentials (v_i) and a set of basis functions for each site for solving the Schrödinger's equations for each v_i. Convenient sources for both are the published tables of Clementi and Roetti[43] and McLean and McLean.[44] These tables contain Slater-type radial functions that can be used to construct sets of basis functions. While this approach gives reasonably good results for various compounds,[33–37] it, nevertheless, has limited variational freedom. Here we employ a procedure for constructing basis functions that removes this limitation. Details of how the bases are constructed are presented below. For now, we drop the site index and assume basis functions of the form

$$\phi_i(\mathbf{r}) = \phi_i(r) Y_{l_i m_i}(\hat{\mathbf{r}}) \tag{20}$$

are given.

Schrödinger's equation for a given atomic site is solved by expressing the wave function as a linear combination of the basis functions, $\psi(\mathbf{r}) = \sum_j c_j \phi_j(\mathbf{r})$, with expansion coefficients (c_j) given by eigenvectors of

$$(\mathbf{H} - \epsilon \mathbf{S})\mathbf{c} = 0, \tag{21}$$

where

$$H_{ij} = \int \phi_i^*(\mathbf{r}) \left[-\frac{1}{2}\nabla^2 + v(\mathbf{r}) \right] \phi_j(\mathbf{r})\, d^3 r \tag{22}$$

and

$$S_{ij} = \int \phi_i^*(\mathbf{r}) \phi_j(\mathbf{r})\, d^3 r \tag{23}$$

are the elements of the Hamiltonian and overlap matrices.

Evaluation of the matrix elements H_{ij} and S_{ij} is straightforward. The kinetic-energy operator in spherical coordinates separates into the familiar radial and angular-momentum operators. Integrations for fixed radius are expressed in terms of the well-known $3j$ coefficients.[45] Radial integrations are carried out as discussed in Appendix B.

Given a set of nonorthogonal basis functions $\phi_i(\mathbf{r})$, the eigenvalue equation

$$\mathbf{S}\mathbf{v} = \lambda \mathbf{v} \tag{24}$$

may be solved to find the eigenvectors,

$$\mathbf{v}(\mathbf{r}) = \sum_i a_i \phi_i(\mathbf{r}), \tag{25}$$

normalized so that

$$\sum_i a_i^* a_i = 1. \tag{26}$$

Since $\mathbf{S}$ is a Hermitian matrix, the eigenvectors are orthogonal,

$$\int \mathbf{v}_i^*(\mathbf{r}) \mathbf{v}_j(\mathbf{r})\, d^3 r = \lambda_i \delta_{ij}. \tag{27}$$

The eigenvalues λ_i indicate how "independent" the basis functions are. An eigenvector with a very small eigenvalue is

a combination of basis functions that nearly add up to zero. This would not be a good combination to use as a basis function. Using it could produce noise in the calculated energy. In general, we discard any eigenvector with an eigenvalue less than a specified basis optimization parameter of $\sim 10^{-5}$. However, if we choose the original set of basis functions carefully, this situation does not arise. A general method for selecting basis functions that avoids this problem is described below.

The Hamiltonian matrix for each nonequivalent atom in the unit cell is computed and diagonalized. Then the lowest-energy levels (eigenvalues, ϵ) for the entire system are occupied by the available electrons. For some systems this may lead to charge transfer among the atoms to avoid having unoccupied (or partially occupied) levels with lower energy than occupied levels. Such transfers are needed to achieve minimum total energy. If a minimum is achieved for fractional-charge transfer, then the two levels involved in the transfer become degenerate at the minimum, in accord with Janak's theorem.[42] This situation rarely occurs for real insulators with ionic bonding, i.e., those systems for which SCAD is expected to be most reliable, so we have not yet adopted an automated method to treat charge transfer. However, in Sec VIA, we do find fractional-charge transfer in SiC but for an unphysically large lattice constant. Once the occupation numbers for the energy levels of each atom are determined, the wave functions are squared, weighted by the occupation numbers and summed to get the total density for each atom. The squared wave functions contain products of two Y_{lm}'s, which are readily converted into a linear combination of single Y_{lm}'s using appropriate $3j$ coefficients. We note that the maximum l in the charge-density expansion is two times the maximum l in the wave function.

A fraction of the new charge density is mixed with the old, new potentials are generated, etc., until convergence is achieved. We find a mixing fraction of 0.4 works well in most cases. The degree of convergence can be determined by comparing occupied eigenvalues with those of the previous cycle. If we define convergence error as the sum of the magnitude of the difference between the new and old occupied eigenvalues, $C_e = \Sigma |\epsilon_n - \epsilon_o|$, then we find the associated numerical error in total energy is typically $\sim 0.001 C_e$. Convergence to $\sim 0.000\,001$ hartree in the total energy is achieved, typically, in about 15–20 iterations.

During the iteration cycles the radial functions in the charge-density expression only need to be determined on the logarithmic mesh. However, extra points are needed in the final iteration to obtain accurate contributions to the energy due to integration over sharp features in $v_L(\mathbf{r})$ and $v_n(\mathbf{r})$. Of course, the radial integrations involving the basis functions must be carried out accurately over the structure in v_L and v_n in each iteration. The sharp features in v_L are determined at the extra points by interpolation from values for the integrals (given in Appendix D) on the logarithmic mesh.

There are several issues to consider in selecting basis functions. Slater-type functions are desirable to obtain the correct analytic behavior of the wave functions near the nucleus. Gaussian-type functions offer greater control for systematically extending coverage away from the nucleus since they fall to zero more rapidly at large r than do Slater

functions. Moreover, we find that Gaussian-type functions tend to give a lower total energy compared to a similar set of Slater-type functions, provided atomic orbitals are included in the basis to get the correct behavior at the nucleus. The problem with including atomic orbitals in the basis is that they may be approximated well by a linear combination of the other basis functions, leading to a nearly singular overlap matrix.

Barnes[46] examined an approach for selecting Slater-type functions in the spherical SCAD approximation that can be systematically expanded to achieve increasingly higher levels of convergence. Here we adopt a similar approach using both Slater- and Gaussian-type functions. Let l_a be the largest value of l for occupied atomic levels, e.g., $l_a = 1$ for oxygen. We let L be the maximum l used in the bases, while $L(X)$ denotes the maximum l used in the basis for element X. Sets of Slater-type functions ($r^l e^{-\beta_i r} Y_{lm}$) or Gaussian-type functions ($r^l e^{-\alpha_i r^2} Y_{lm}$) are chosen to be "even tempered." That is, β_{i+1} / β_i (or α_{i+1} / α_i) are constant, which follows from requiring a constant overlap, or temperament, t, between adjacent functions in a normalized set,

$$t = 4\pi \int_0^\infty r^2 \phi_i(r) \phi_{i+1}(r) d^3 r. \tag{28}$$

For $l \leq l_a$ we select a Slater-type function with $\beta_1 = Z/(l+1)$, which is suggested by the analytic form of hydrogenlike wave functions. Optimized Slater-type bases for atoms generally include somewhat larger values for β as well; thus we also include the $i = 0$ function ($\beta_0 > \beta_1$) in our basis. Successively smaller values of β may be included until convergence is achieved. It is convenient to relate the values of β to the region of space where they contribute most. For Slater functions this corresponds to the peak of $r^{2l+2} e^{-2\beta r}$, which occurs at $r = (l+1)/\beta$. Thus, the smallest value of β in a set belonging to l is given by a maximum radius, which we call the orbital cutoff radius, r_c. Analogous sets of Gaussian-type orbitals are defined by requiring the $i = 1$ functions to have their peaks at the same radii as the $i = 1$ Slater-type functions [$\alpha_1 = \beta_1^2 / 2(l+1)$] as well as the same values of t and r_c for both types. For $l \leq l_a$ we choose two Slater-type functions ($i = 0, 1$) and Gaussian-type functions for $i \geq 2$. For $l > l_a$, we use only Gaussian-type functions, with minimum peak radius corresponding to that of the Slater-type function with $\beta = \beta_1$ and $l = l_a$. We find that adequate values for t lie in the range of $0.8 < t < 0.9$ for $l \leq l_a$ and $0.7 < t < 0.8$ for $l > l_a$.

The total number of basis functions can be decreased without significant loss in accuracy by increasing the minimum peak radius for functions with $l > l_a$ to a value near the radius of the peak in the wave function for the highest-energy occupied levels. However, to simplify the presentation in this paper, we keep the extra basis functions in the core region and, unless otherwise stated, we use $t = 0.9$ for $l \leq l_a$ and $t = 0.8$ for $l > l_a$.

Another related parameter to consider is the maximum l allowed in the potential L_v. The SCAD code is currently limited to $L_v \leq 12$. If $L_v = 0$ then we force the ions to be spherical and SCAD becomes the spherical SCAD model.[28] In principle, L_v can be twice L, for example, due to the

contributions to the electrostatic potential from on-site electrons since maximum l in the charge-density expansion is $2L$. On the other hand, allowing L_v to become large without constraint can lead to poor convergence with increasing L. We believe this is due to dissatisfaction of Schrödinger's equation,

$$H\psi(\mathbf{r}) = -\frac{1}{2}\nabla^2\psi(\mathbf{r}) + v(\mathbf{r})\psi(\mathbf{r}) = \mathcal{E}\psi(\mathbf{r}), \qquad (29)$$

for the higher l values. The maximum l in the $\nabla^2\psi$ term is L and the maximum l in the $\mathcal{E}\psi$ term is L, while the maximum l in the $v\psi$ term is $3L$. Clearly, any terms in $v\psi$ with $l > L$ contribute to a dissatisfaction of the Schrödinger equation. One can remove this source of error by setting to zero those $3j$ coefficients that contribute to terms with $l > L$ in the spherical harmonic expansion of $v\psi$. However, this means that L must be quite large to allow significantly large values of L_v. (For example, if $L = 10$ the maximum l contribution from the potential is $L_v = 6$.) The greater amount of time needed to diagonalize the larger Hamiltonian matrices required using this approach tends to spoil the overall efficiency of the SCAD method. On the other hand, if contributions from the potential are not limited, obtaining convergence with respect to the increasing L can be difficult.

A more practical approach can be found which incorporates the full potential at a faster pace with increasing L and still limits errors from the dissatisfaction of Schrödinger's equation. The maximum l values for spherical harmonic expansions of the terms in $\psi^*(\mathbf{r})(H-\mathcal{E})\psi(\mathbf{r})$ are $2L$ for the $\psi^*\nabla^2\psi$ term, $4L$ for the $\psi^*v\psi$ term, and $2L$ for the $-\psi^*\mathcal{E}\psi$ term. In this approach we limit contributions to matrix elements involving the potential that give terms in $\psi^*v\psi$ with $l > 2L$.

The product of three $Y_{l,m}$'s may be written as a sum of single $Y_{l,m}$'s with real $(4j)$ coefficients, and the coefficient of the $Y_{0,0}$ term gives the integral of that product over all solid angle, which is, of course, the $3j$ coefficient. Only a few percent of $Y_{l,m}$ triplets have nonzero $3j$ coefficients and thus contribute to H. This number can be further reduced by setting to zero those with $l_v > L$, or still further reduced, by requiring $l_i + l_j + l_v < 2L$. The latter condition also implies $l_v \leq L$. It also demands that the $Y_{l,m}$ expansion of a $Y_{l,m}$ triplet has no terms with $l > 2L$, which must be the case for precise satisfaction of $\psi^*(\mathbf{r})(H-\mathcal{E})\psi(\mathbf{r}) = 0$. We find only small differences between results obtained using the $l_v \leq L$ and $l_i + l_j + l_v < 2L$ constraints. Neither constraint is as strict as the one based on $(H-\mathcal{E})\psi(\mathbf{r}) = 0$, but they offer a faster convergence with increasing L due to the greater allowed values of L_v. Convergence can be made smoother by scaling the potential for l_v near L_v; for example, by analogy with the practice of using a Fermi function to incorporate states near the Fermi level in a KS calculation. Unless otherwise stated, results reported here use the least restrictive $l_v \leq L = L_v$ constraint with a scale factor of 0.5 for $l_v = L_v$.

C. Total energy

The total energy as expressed in Eq. (1) is deceptively simple looking. While the actual calculation of U is straight-

forward, it is conceptually more difficult because it must be expressed in terms of the self-consistent charge densities n_i and the potentials v_i as they are formulated in Sec IIIA. Having the total charge density decomposed into contributions from each atomic site allows the same decomposition of the total energy: $U = \Sigma_i U_i$, where the sum is over all atoms in the system. This decomposition is obvious for the electrostatic contributions but, perhaps, less obvious for the kinetic and exchange-correlation energies. To illustrate this point, consider the only the kinetic-energy contribution from the second term in Eq. (4). The first and third terms are already site decomposed. Let e_k be the energy density functional corresponding to T_k. (If T_k is the Thomas-Fermi function then $e_k = An^{2/3}$.)

$$T_k[n(\mathbf{r})] = \int n(\mathbf{r})e_k[n(\mathbf{r})]d^3r, \qquad (30)$$

where the integration is over all space. After substituting Eq. (2) and interchanging the sum and integration, we have

$$T_k[n(\mathbf{r})] = \sum_i \int n_i(\mathbf{r} - \mathbf{R}_i)e_k[n(\mathbf{r})]d^3r. \qquad (31)$$

In the final iteration of SCAD $e_k[n(\mathbf{r})]$ is computed separately for each atomic site in terms of $\mathbf{r} - \mathbf{R}_i$. In other words, $e_k(\mathbf{r} - \mathbf{R}_i)$ is an accurate representation of $e_k[n(\mathbf{r})]$ in the region $|\mathbf{r} - \mathbf{R}_i| < R_c$. Making this substitution yields the desired form,

$$T_k[n(\mathbf{r})] = \sum_i \int n_i(\mathbf{r} - \mathbf{R}_i)e_k(\mathbf{r} - \mathbf{R}_i)d^3r. \qquad (32)$$

An analogous expression is obtained for $U_{xc}[n(\mathbf{r})]$. If our system is a crystal, then the sum over i can be limited to one structural unit, or unit cell, containing N atoms, and

$$U = \sum_i^N U_i \qquad (33)$$

is the energy per unit cell. Of course, the values for U_i do *not* depend on the infinitely many choices for lattice vectors and basis vectors available to uniquely define a crystal structure. Likewise, the values of the U_i do *not* depend on any particular region of space that could be selected to represent the unit cell. This is because integrations required to compute U_i are carried out *over all space* and not over some selected finite region of space. We emphasize this point, hopefully, to clarify confusion about the capability of models such as SCAD to give well defined results for polarization and related properties.[39]

We calculate the energy associated with each site by evaluating the expression

$$U_i = -\frac{1}{2}\sum_\alpha o_{\alpha,i} \int \psi_{\alpha,i}^*(\mathbf{r})\nabla^2\psi_{\alpha,i}(\mathbf{r})d^3r + \int n_i(\mathbf{r})e_1^{(i)}(\mathbf{r})d^3r$$

$$+ \int n_i(\mathbf{r})e_2^{(i)}(\mathbf{r})d^3r + \frac{1}{2}Z_i\{v_p^{(i)}(0) - v_n^{(i)}(0)$$

$$- \sum_j{}' v_H^{(j)}(-\mathbf{R}_j)\}, \tag{34}$$

where $o_{\alpha,i}$ is the number of electrons in the αth state of the ith atom. All functions of $\mathbf{r}$, as well as the neighboring positions $\mathbf{R}_j$, are expressed with respect to an origin at $\mathbf{R}_i$. The energy density in the second line is separated into two terms, $e_1^{(i)}$ and $e_2^{(i)}$, to emphasize the two types of quadrature that are needed for contributions that are smooth at neighboring sites and contributions which have discontinuous derivatives at neighboring sites. The sum of contributions designated on site, smooth, and poles give e_1, while the sum of Löwdin and nuclear contributions give e_2. Specifically,

$$e_1^{(i)}(\mathbf{r}) = \frac{1}{2}\int \frac{n_i(\mathbf{r}')}{|\mathbf{r} - \mathbf{r}'|}d^3r' - \frac{Z_i}{r} + e_{xc}[n_i(\mathbf{r})] + e_{ov}[n(\mathbf{r})]$$

$$- e_{ov}[n_i(\mathbf{r})] - \sum_j{}'\left\{ e_{ov}[n_0^{(j)}(|\mathbf{r} - \mathbf{R_j}|)] + \frac{1}{2}v_H[n_j(\mathbf{r}]\right.$$

$$\left. - \mathbf{R}_j)] - \frac{1}{2}v_H[n_0^{(j)}(|\mathbf{r} - \mathbf{R_j}|)]\right\} + \frac{1}{2}v_p^{(i)}(\mathbf{r}) \tag{35}$$

and

$$e_2^{(i)}(\mathbf{r}) = \sum_j{}'\left\{ e_{ov}[n_0^{(j)}(|\mathbf{r} - \mathbf{R_j}|)] + \frac{1}{2}v_H[n_0^{(j)}(|\mathbf{r} - \mathbf{R_j}|)]\right\}$$

$$+ \frac{1}{2}v_n(\mathbf{r}), \tag{36}$$

where, as in Sec. III B, $\sum_j{}'$ implies the $j=i$ term and terms with $|\mathbf{R}_i - \mathbf{R}_j| > R_c$ are omitted. The factor $\frac{1}{2}$ multiplies contributions from v_H and v_p to avoid double counting the electron-electron energy. Note that v_p also contains contributions from the nuclei, originating from the monopoles. Thus, the contribution from the ith electrons interacting with nuclei outside R_c is only half included through the v_p term. The other half is included by the v_p term in Eq. (34).

D. Forces

The above expressions for total energy illustrate details involved in the way we actually compute the energy. Now we write the total energy in a form more convenient for discussing forces. The energy for the entire collection of atoms is written as

$$U[n(\mathbf{r})] = -\frac{1}{2}\sum_{\alpha,i}\int \psi_{\alpha,i}^*(\mathbf{r})\nabla^2\psi_{\alpha,i}(\mathbf{r})d^3r$$

$$+ \frac{1}{2}\sum_{i,i'}\int \frac{n_i(\mathbf{r})n_{i'}(\mathbf{r}')}{|\mathbf{r} - \mathbf{r}'|}d^3r d^3r' + \sum_i \int (e_k[n(\mathbf{r})]$$

$$+ e_{xc}[n(\mathbf{r})] - e_k[n_i(\mathbf{r})])n_i(\mathbf{r})d^3r$$

$$- \sum_{i,i'}\int \frac{Z_{i'}n_i(\mathbf{r})}{|\mathbf{r} - \mathbf{R}_{i'}|}d^3r + \frac{1}{2}\sum_{i,i'}\frac{Z_iZ_{i'}}{|\mathbf{R}_i - \mathbf{R}_{i'}|}, \tag{37}$$

where Σ_α includes only occupied levels and, for simplicity, we assume each level is occupied by one electron. Applying the definition of force on the jth atom,

$$\mathbf{F}_j \equiv -\frac{\partial U[n(\mathbf{r})]}{\partial\mathbf{R}_j}, \tag{38}$$

to the energy expression in Eq. (37), we find

$$\mathbf{F}_j = \frac{1}{2}\sum_{\alpha,i}\int \left(\frac{\partial\psi_{\alpha,i}^*}{\partial\mathbf{R}_j}\nabla^2\psi_{\alpha,i} + \frac{\partial\psi_{\alpha,i}}{\partial\mathbf{R}_j}\nabla^2\psi_{\alpha,i}^*\right)d^3r$$

$$+ \sum_i\int (-v_{es}(n) - v_k(n) - v_{xc}(n) + v_k(n_i))\frac{\partial n_i}{\partial\mathbf{R}_j}d^3r$$

$$+ Z_j\sum_i\left(-\int \frac{(\mathbf{r} - \mathbf{R}_j)n_i}{|\mathbf{r} - \mathbf{R}_j|^3}d^3r + \frac{Z_i\mathbf{R}_j}{|\mathbf{R}_i - \mathbf{R}_j|^3}\right), \tag{39}$$

where the Green's theorem has been applied to the second term involving ∇^2, the Hartree and external potentials are combined in $v_{es}(n)$, expressions for functional derivatives $[v(n) = e'(n)n + e(n)]$ are employed, and, for simplicity, the dependence of n and n_i and ψ on $\mathbf{r}$ is not shown. The last term is recognized as the Z_j times $\mathbf{E}_j$, the electric field at R_j, and the sum of potentials in the second line is simply v_i. Thus, substituting $n_i = \Sigma_\alpha\psi_{\alpha,i}^*\psi_{\alpha,i}$ we have

$$\mathbf{F}_j = \frac{1}{2}\sum_{\alpha,i}\int \left(\frac{\partial\psi_{\alpha,i}^*}{\partial\mathbf{R}_j}\nabla^2\psi_{\alpha,i} + \frac{\partial\psi_{\alpha,i}}{\partial\mathbf{R}_j}\nabla^2\psi_{\alpha,i}^*\right)d^3r$$

$$- \sum_{\alpha,i}\int v_i(\mathbf{r})\left(\frac{\partial\psi_{\alpha,i}^*}{\partial\mathbf{R}_j}\psi_{\alpha,i} + \psi_{\alpha,i}^*\frac{\partial\psi_{\alpha,i}}{\partial\mathbf{R}_j}\right)d^3r + Z_j\mathbf{E}_j. \tag{40}$$

If we add

$$0 = \sum_{\alpha,i}\frac{\partial}{\partial\mathbf{R}_j}\int \psi_{\alpha,i}^*\psi_{\alpha,i}d^3r \tag{41}$$

and set $-\frac{1}{2}\nabla^2 + v_i = H_i$, then we have

$$\mathbf{F}_j = \Re\left\{ -2\sum_{\alpha,i}\int \frac{\partial\psi_{\alpha,i}^*}{\partial\mathbf{R}_j}(H_i - \epsilon_{\alpha,i})\psi_{\alpha,i}d^3r\right\} + Z_j\mathbf{E}_j. \tag{42}$$

If Schrödinger's equations are satisfied everywhere, then $\mathbf{F}_j$ is just the Hellman-Feynman[47,48] force, $Z_j\mathbf{E}_j$. The first term is analogous to the Pulay[49,50] correction of the KS formulation and may be further developed by substituting the expanded form of the wave function, $\psi_{\alpha,i} = \Sigma_k c_{\alpha,k}^{(i)}\phi_k^{(i)}$. We find

$$\mathbf{F}_j = -2\Re\left\{ \sum_{\alpha,i,k}\frac{\partial c_{\alpha,k}^{(i)*}}{\partial\mathbf{R}_j}(\mathbf{H}_i - \epsilon_{\alpha,i}\mathbf{S}_i)\mathbf{c}_\alpha^{(i)} + \int c_{\alpha,k}^{(i)*}\frac{\partial\phi_k^{(i)*}}{\partial\mathbf{R}_j}\right.$$

$$\left. \times(H_i - \epsilon_{\alpha,i})\psi_{\alpha,i}d^3r\right\} + Z_j\mathbf{E}_j. \tag{43}$$

The first term is zero from Eq. (21) and the second term is zero unless $i=j$. Thus, we have

$$\mathbf{F}_j = -2\Re\left\{\int \Phi_{\alpha,j}^*(H_j - \epsilon_{\alpha,j})\psi_{\alpha,j}d^3r\right\} + Z_j\mathbf{E}_j, \quad (44)$$

where

$$\Phi_{\alpha,j} = \sum_k c_{\alpha,k}^{(j)}\frac{\partial \phi_k^{(j)}}{\partial \mathbf{R}_j}. \quad (45)$$

Having eliminated the $i \neq j$ terms, we find it more convenient to work with Eq. (42). The terms involving $\epsilon_{\alpha,i}$ turn out to be zero, and those involving H_i are real, so we have, finally,

$$\mathbf{F}_j = -2\sum_\alpha \int \frac{\partial \psi_{\alpha,j}^*}{\partial \mathbf{R}_j}H_j\psi_{\alpha,j}d^3r + Z_j\mathbf{E}_j. \quad (46)$$

IV. SOME SIMPLE MOLECULES

The purpose of this section is to demonstrate two important features of SCAD using results for some simple molecules. (1) For a few nontrivial systems the SCAD and KS methods are equivalent because of zero overlap charge density. For these systems SCAD succeeds by putting the charge of one atom at the nucleus of another. (2) For other (most) systems the repulsive potential derived from the overlap kinetic energy prevents SCAD from putting the charge density associated with one atom near the nucleus of another.

Obviously, SCAD can be applied to molecules as well as solids. For molecules such as HF, CH_4, and H_2O, the SCAD and KS methods become equivalent. For these systems the lowest-energy eigenvalue at the H site is higher than the highest occupied level of the F, C, or O sites. Thus, SCAD insists on treating these molecules as F^{-1}, C^{-4}, and O^{-2} ions in the presence of one, four, and two proton potentials, respectively. Since the protons have no electrons, the T_k overlap term does not contribute to the energy and the SCAD and KS methods become equivalent. If the protons are moved far enough away from their equilibrium positions near the negative ions, at some point, it becomes energetically favorable for charge to flow back to the proton to form the hydrogen atom. This charge-flow effect and the convergence of SCAD-derived properties to the results obtained from the KS method are demonstrated in the work of Ossowski et al.[40] for the H_2O molecule.

In general, SCAD calculations do involve T_k. Thus, unless T_k is the divine functional, a SCAD calculation does not converge to the KS result. While the basis functions on a given site may be sufficiently general to move charge to a neighboring site, this is prevented by the T_k contribution to the overlap potential. To illustrate this, consider a pair of He atoms, say, He1 and He2. For the sake of discussion, suppose that we can put a complete set of basis functions centered on either He1 or He2 or both. Then, in principle, we could use the complete basis on either He1 or He2 and achieve the KS result by treating the He pair as a He^{-2} ion (say, He1) in the presence of a He^{+2} potential (He2). The lowest energy-eigenvalues would be nearly fourfold degenerate, corresponding to the two doubly degenerate $1s$ levels of He. Two of the wave functions would be centered on the He1 and two would be centered around He2, even though, formally, all
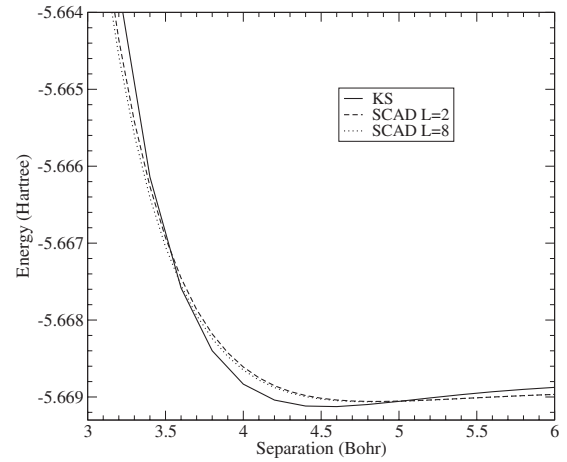
FIG. 1. Total energy U as a function of interatomic separation for a helium atom pair, obtained using the KS code NRLMOL and the SCAD method with $L=2$ and $L=8$.

four would be associated with He1. There would be no T_k contribution simply because we chose to associate all the charge with He1.

Next, we attempt to illustrate these points with specific results for the helium atom pair. In Fig. 1 the KS results for energy versus atom separation are compared with SCAD results for $L=2$ and $L=8$. The KS calculations were carried out using the code NRLMOL.[51–57] Both methods used the Perdew and Wang[58] local-density approximation (LDA) for exchange and correlation. The NRLMOL He basis is constructed from local s-, p-, and d-type Gaussian-based orbitals. The decay parameters are optimized as discussed by Porezag and Pederson[59] with the smallest value of $0.183/\text{bohr}^2$. For comparison the smallest SCAD decay parameter is $0.014/\text{bohr}^2$.

The outer most peak for the SCAD bases is at $r_c=6$ to ensure sufficient overlap of basis functions with the neighboring atom. SCAD results for $L=6$ are indistinguishable from those for $L=8$ on the scale in Fig. 1. We note that the $L=2$ and $L=8$ results merge together at large separation, as expected, when the atoms become nearly isolated from each other. For large separation the SCAD values are a little lower in energy than the KS values, which implies that, for isolated atoms, the SCAD basis is slightly superior to that selected for the KS calculation. In general, the KS results are more accurate than SCAD. Thus, the lower energy SCAD values at small separation are due to the T_k approximation. Actually, neither method is very accurate for the helium pair because they both neglect the van der Waals interaction.

We may transfer charge from one atom to another by simply changing the eigenvalue occupation numbers from that of the ground state. Of course, if charge is moved to a higher energy level, the total energy will increase. For this illustration the interatomic separation is fixed at 4 bohr. With two electrons on each atom, the two lowest SCAD eigenvalues are $-0.569\,73$ and $0.007\,78$ for $L=2$ and $-0.569\,89$ and $0.007\,21$ for $L=8$. For comparison, the three lowest KS values are $-0.586\,04$, $-0.554\,62$, and $0.199\,54$. Clearly, U will increase as electronic charge is taken from the $\sim\!-0.57$ energy state to the $\sim\!0.01$ energy state because, to achieve minimum U, one must occupy the lowest-energy states of the
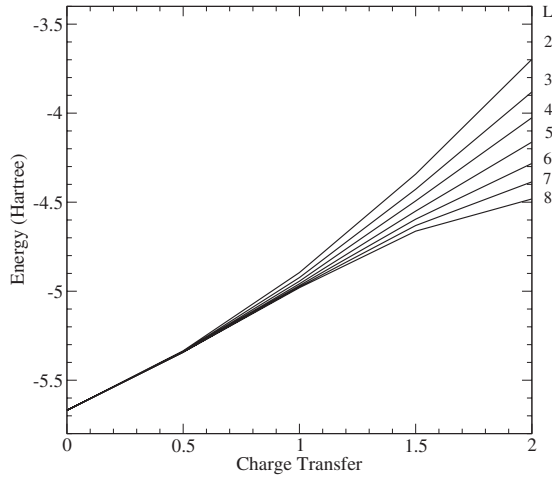
FIG. 2. SCAD values for U as a function of charge transfer from one atom to the other in a helium atom pair with interatomic separation of 4 bohr.

system. On the other hand, if both electrons are transferred, the T_k term becomes zero, and, in principle, SCAD should give the KS result. In practice, the bases we use are not general enough for this to happen accurately, but we can illustrate the trend.

In Fig. 2 U is shown as a function of charge transfer from one helium to the other. For small charge transfer there is little change in U with increasing L and SCAD rapidly converges to a result for U and charge density that is uniquely governed by T_k. If T_k were the divine functional, then the SCAD value for U and the total charge density would equal the KS result, even though the occupied eigenvalues for SCAD and KS would differ. For our example, the two occupied KS eigenvalues differ by 0.031 hartree, while the two occupied SCAD eigenvalues (one for each site) are necessarily equal by symmetry. At the other extreme, when all charge is transferred to one atom, U is lowered with increasing L as the charge assigned to one atom is placed at the other atom owing to increasing flexibility in the basis gained by increasing L. The second lowest occupied energy level, which had the value ~ 0.07 for zero charge transfer, becomes ~ -0.20 for $L=2$ and ~ -0.36 for $L=8$, presumably headed for the KS value of ~ -0.55 as $L \rightarrow \infty$ and radial part of the basis functions become complete. Somewhere between zero ($q=0$) and complete ($q=2$) charge transfer, the converged SCAD $U(q)$ has a maximum at the crossing of the lowest eigenvalue of He^{+q} and the second-lowest eigenvalue of He^{-q}, in accord with Janak's theorem.

The charge-transfer effect is further illustrated in Fig. 3 where the electron density is plotted as a function of position along the line passing through the two nuclei. With no charge transfer any changes in the densities with increasing L are not distinguishable on the scale in Fig. 3. Clearly, it is the potential due to T_k that keeps the ith charge on the ith atomic site because the basis is flexible enough to move charge to the neighboring site if that is required to lower the energy. This is apparent, from the fact that when we artificially assign all charge to one nucleus, charge moves back to the bare nucleus, increasingly, as L increases.
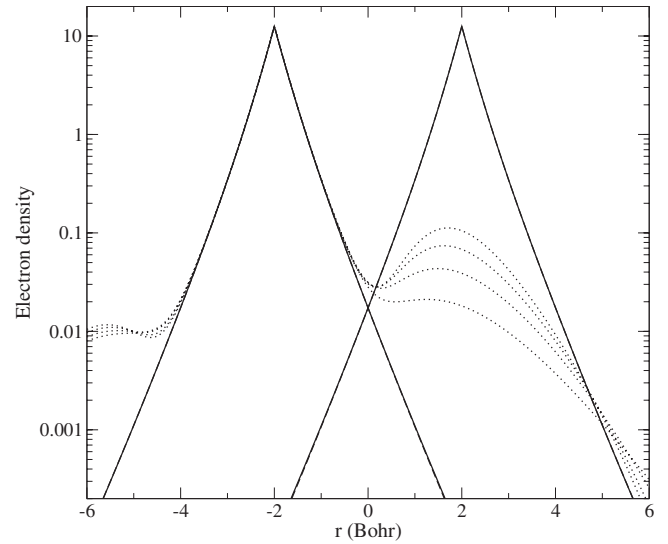
FIG. 3. Electron density for a pair of helium atoms as a function of position along the bond direction, r. Nuclei are at $r \mp 2$. The solid lines give the two SCAD atom densities with zero charge transfer using $L=6$. The dotted lines denote results when two electrons are transferred from the atom at $r=2$ to the one at $r=-2$ with $L=2$, 4, 6, and 8 showing increasing amount of charge moved back the $r=2$ nucleus.

In summary, the SCAD method formally becomes the KS method when $T_k=0$, as one would expect, and in practice, they give the same answer as the set of basis functions becomes complete. However, for $T_k \neq 0$, SCAD results do not necessarily approach KS results as the bases become complete. The SCAD basis functions may be general enough to move charge to neighboring sites, but the potential due to T_k can prevent that from happening, no matter how complete the basis. SCAD converges to a unique result determined by T_k. If T_k is divine, the U and the total charge density agree with a KS calculation, by definition. If T_k is less than divine, SCAD results differ from KS results, and the discrepancies are a measure of the error resulting from the approximation for T_k.

V. ALUMINUM FLUORIDE

In this section we analyze results of SCAD applied to AlF_3. Fluorides are ideal compounds on which to test SCAD because they have the least amount of covalent-type bonding in a KS calculation. Moreover, AlF_3 provides an interesting test for DFT methods in general, owing to the presence of a structural transition that is quite sensitive to volume. This was emphasized in a recent paper,[41] which included SCAD calculations based on the strictest Schrödinger equation constraint discussed in Sec. III B. As expected, the lowest energy electronic configuration for AlF_3 occurs when three electrons transfer from aluminum to the three fluorine atoms to form Al^{+3} and F^{-1} ions.

A. Convergence

The cubic phase of AlF_3 has the ReO_3 or $D0_9$ structure. It has a simple-cubic lattice with aluminum ions at the cube
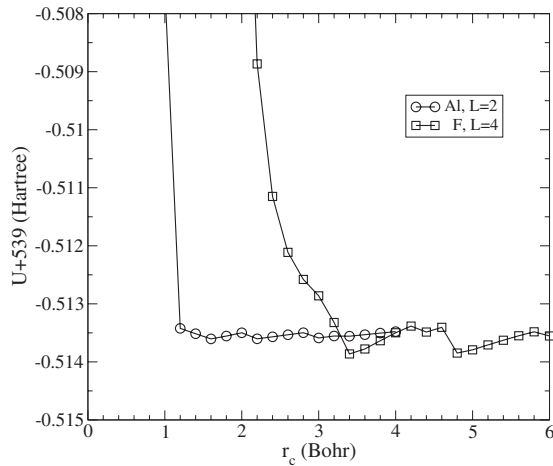
FIG. 4. Total energy U for AlF$_3$ in the cubic structure (a =6.76) as a function of cutoff radius r_c for aluminum bases (circles, L=2) and fluorine bases (squares, L=4). For the aluminum curve, r_c=4 was used for the fluorine basis, and for the fluorine curve r_c=2 was used for the aluminum basis.

FIG. 5. Total energy U for AlF$_3$ in the cubic structure, with a =6.76, as a function of cutoff radius R_c. The left-hand-side scale is for the L=4 results and the right-hand-side scale is for the L=6 results.

center and fluorine ions on the cube faces—like the perovskite structure but without cube-corner ions. Obviously, we would like to choose r_c as small as possible without significantly affecting the results. The total energy U is found to converge abruptly with increasing cutoff radius r_c. This is illustrated in Fig. 4. Clearly, the aluminum basis is converged for $r_c > 1.3$ and the fluorine basis is converged for $r_c > 3.4$. Curves for aluminum bases are identical on this scale for all $L \geq 1$. The small value of r_c for converged aluminum bases results from the fact that the highest occupied level is the Al(2p) state, which is more than 2 hartree lower than the highest occupied level of the system, a fluorine 2p level. As a result, the Al^{+3} ion is small and spherical in shape. The relatively small variations in U beyond the converged values for r_c result from small differences in the bases. As r_c increases, the number of radial functions must increase by one at some point to maintain (approximately) the designated value of t. Small variations in U resulting from such changes in the basis are negligible when considering energy differences due to structural variations.

Another convergence issue to consider is the cutoff radius R_c, beyond which the potential can be treated as point multipoles. Generally speaking, we find R_c must be about two times the minimum acceptable value of r_c for the largest ion, F^{-1} in our case. This is illustrated in Fig. 5, where U is plotted as a function of R_c. In this figure L refers to the bases for fluorine. Both curves employ (L=2 and r_c=2) for aluminum and r_c=4 for fluorine. Change in these parameters within the tolerances shown in Fig. 4 does not produce any significant change in the results shown in Fig. 5. Clearly, at least 24 neighbors must be contained within R_c to obtain acceptable results. The transition to 40, 52, 62, 78, and 86 neighbors results in changes of approximately 11, 7, 5, 5, and 2 μhartree, respectively. The SCAD program can apply structural distortions keeping a fixed neighbor list or allow it to change with the distortion. Subsequent results for AlF$_3$ use R_c sufficient to contain 40 (36) neighbors for fluorine (aluminum) ions, although larger values were applied to test key results.
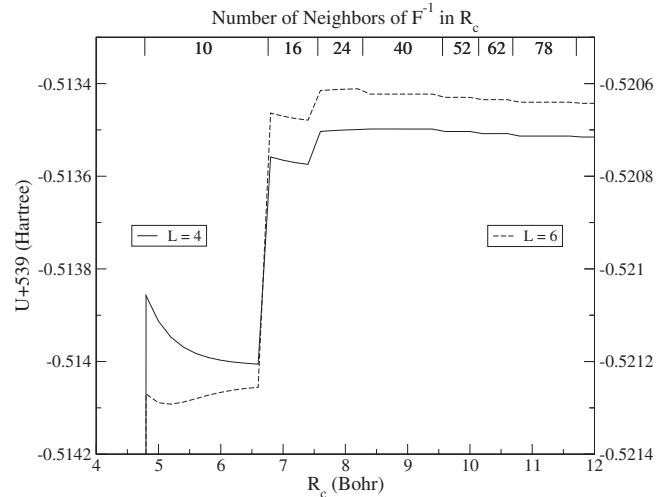
Next we consider convergence of U as regards numerical integrations over solid angles (see Appendix B). To illustrate this type of convergence we focus on the U as a function of volume, or equation of state, for a selected value of L. The equation of state for L=6 is plotted in Fig. 6 using several different values of N_Ω to demonstrate convergence with increasingly accurate Ω quadrature. We find that N_Ω=146 is adequate for most purposes. Subsequent results for AlF$_3$ were obtained using N_Ω=194.

The final convergence issue relates to how SCAD results depend on increasing values for L. This is examined below with the main focus on structural distortions associated with the phase transition in AlF$_3$. Fortunately, we find that reasonably accurate results are achieved for L values of about 4 or 5, for which the Hamiltonian matrices have a rank just 200 or 300. Thus one could begin to address more complicated
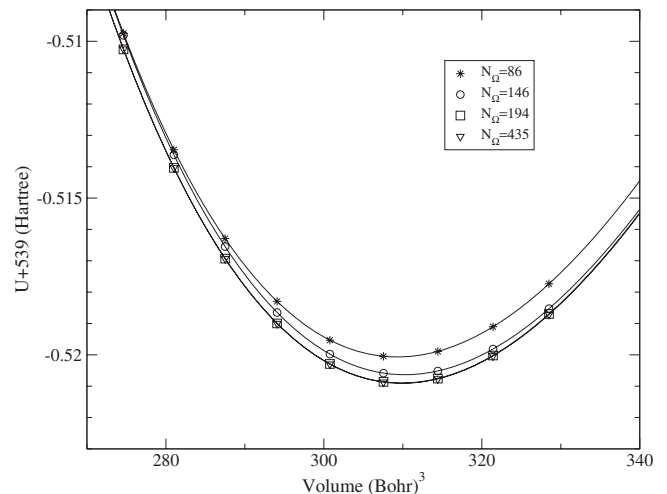
FIG. 6. SCAD (L=6) results for the equation of state of AlF$_3$ in the cubic structure using several different values of N_Ω, the number of directions included in the solid angle quadrature.
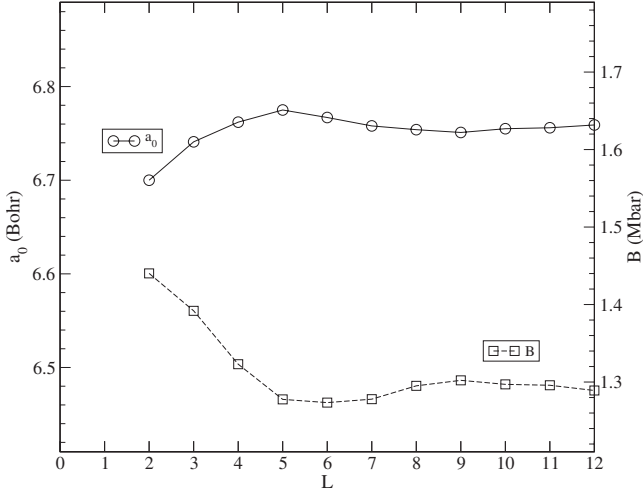
FIG. 7. SCAD results for the equilibrium lattice parameter a_0 and bulk modulus B of AlF$_3$ in the cubic structure as a function of L.

FIG. 8. SCAD results for the Born effective charges $Z^*(F_I)$ and $Z^*(F_{II})$ and the high-frequency dielectric constant ϵ_∞ as a function of L using equilibrium values of a_0 (Fig. 7).

issues, such as surface effects related to catalysis, with relative ease. We believe that using much greater L values would be unlikely to give more accurate results unless higher order corrections to the Thomas-Fermi functional were also included.

B. Cubic structure results

The equilibrium lattice parameters a_0 and bulk modulus B

$$B \equiv V \frac{d^2U}{dV^2} \qquad (47)$$

for the cubic structure are shown in Fig. 7 as a function of L. The small differences compared with those previously published[41] result from the different L_v constraints employed, as discussed in Sec IIIB.

Next we consider polarization induced by an electric field and by the displacement of ions. It is a simple matter to compute the polarization, or, strictly speaking, the change in polarization, when the total charge density is expressed as a sum over contributions from ions with fixed monopoles.[39] This is the case for the SCAD description of the charge density in AlF$_3$. The Born effective charge matrix is defined by

$$Z^*_{\alpha\beta}(k) \equiv V \frac{\partial P_\alpha}{\partial u_\beta(k)}, \qquad (48)$$

where P_α is the αth component of the polarization and $u_\beta(k)$ is the βth component of the displacement of the kth atom.

The high-frequency dielectric constant ϵ_∞ is calculated following the method used in the previous SCAD calculations.[34,35] Specifically, we compute the polarization (**P**) induced when a constant electric field (**E**) term is added to the potential of each atom in the unit cell. This simple "one-cell" approach was found to give reasonably good values for ϵ_∞ with susceptibility given simply by **P**$=\chi$**E**, where **E** is the external, or applied, constant field. In reality, of course, **E** needs to be the total macroscopic electric field. In

the one-cell approach, one can argue that any contributions to the total electric field arising from induced polarization are effectively removed by periodic boundary conditions. Any complications arising from the constant field are nullified by having a basis with limited radius. A more rigorous approach would be to apply an electric field to a finite sized crystal or apply an electric-field wave. In either case the total macroscopic field would then include contributions from the induced polarization.

Results for Z^* and ϵ_∞ are shown in Fig. 8. The two nonzero elements of Z^* for the fluorine ion are denoted by $Z^*(F_I)$ and $Z^*(F_{II})$ where I (II) indicates motion perpendicular (parallel) to nearest aluminum neighbor direction. We find results for $Z^*(Al)$ (not shown) obey the sum rule $Z^*(Al)=-2Z^*(F_I)-Z^*(F_{II})$ to within about ±0.003. These quantities are needed to calculate optic mode frequencies in the long-wavelength limit.

C. Phonons in cubic AlF$_3$

In this section we report results obtained using the SCAD program and the frozen-mode package FROZSL (Ref. 60) to compute phonon frequencies. The FROZSL code uses the database of Stokes and Hatch[61] to determine the simplest structural distortions required to compute energy differences needed to calculate phonon frequencies for any selected irreducible representation. Here we limit ourselves to modes with wave vectors **q** at the Γ, X, M, and R points in the Brillouin zone. The nonregular part of the dynamical matrix[1,62,63] is automatically included in the Γ phonon mode calculation if the Z^* and ϵ_∞ matrices and the wave vector direction are provided as input to FROZSL. The nonregular contribution splits the threefold degenerate Γ_4^- mode into a twofold-degenerate transverse optic (TO) mode and a singly degenerate longitudinal-optic (LO) mode. Daniel *et al.*[64] employed a rigid-ion (RI) model, with parameters chosen to fit Raman frequencies in the low-temperature phase, to calculate phonon-dispersion curves for AlF$_3$ in the cubic phase. Zinenko and Zamkova[65] reported dispersion curves based on the parameter-free extended Gordon-Kim model of Ivanov

TABLE I. Frequencies (in cm^{-1}) for AlF$_3$ in the cubic structure at the Γ, R, M, and X points of the Brillouin zone: from the SCAD, RI (Ref. 64), and PPIB (Ref. 65) models. Irreducible representation labels are those of Miller and Love (Ref. 66) (ML) with degeneracies in parentheses.

	Γ				R		
ML	SCAD	RI	PPIB	ML	SCAD	RI	PPIB
$4^-(2)$	275 ± 14	375	222	$5^+(3)$	516 ± 12	445	485
LO(1)	510 ± 4	475	307	$2^-(1)$	718 ± 6	670	645
$4^-(2)$	586 ± 17	650	521	$3^-(2)$	396 ± 24	475	372
LO(1)	690 ± 17	770	651	$4^-(3)$	332 ± 4	380	246
$5^-(3)$	200 ± 4	225	194	$5^-(3)$	$56i \pm 13i$	50	58
	M				X		
ML	SCAD	RI	PPIB	ML	SCAD	RI	PPIB
$1^+(1)$	336 ± 4	400	250	$1^+(1)$	255 ± 4	275	225
$2^+(1)$	$54i \pm 14i$	50	65	$1^+(1)$	578 ± 10	660	525
$3^+(1)$	396 ± 24	480	370	$2^+(1)$	208 ± 5	225	205
$4^+(1)$	671 ± 9	625	520	$5^+(2)$	107 ± 5	110	115
$5^+(2)$	228 ± 4	250	205	$5^+(2)$	254 ± 11	330	225
$2^-(1)$	190 ± 10	220	185	$5^+(2)$	577 ± 18	640	520
$2^-(1)$	574 ± 20	645	585	$3^-(1)$	609 ± 12	570	475
$5^-(2)$	232 ± 6	255	210	$5^-(2)$	229 ± 8	250	200
$5^-(2)$	536 ± 11	540	455				

and Maksimov,[23] which has polarizable ions and potential induced breathing (PPIB). They found $\epsilon_\infty = 1.86$ and fluorine Z^* values of -0.66 and -1.76, which are close to our values (Fig. 8). Our results for phonon frequencies at symmetry points in the Brillouin zone are compared with those of the RI and PPIB models in Table I. The SCAD results are the average of $L=4$ 5, 6, and 7 values, obtained using the equilibrium lattice parameters (Fig. 7) and the $\pm$ uncertainties give the maximum difference found among the four averaged values. Other numerical uncertainties within SCAD are expected to be less than that produced by the variation in L.

The comparison of frequencies among the models is reasonably good except for the fact that the RI and PPIB models have soft, but stable, M_2^+ and R_5^- modes, while SCAD produces unstable values for these modes. The frequency of these soft and/or unstable modes depends strongly on volume. Thus, the error in the frequency of these modes may be attributed to a corresponding error in the equilibrium volume.[41]

D. Low symmetry structure of AlF$_3$

The unstable R_5^- mode may "freeze" into lower symmetry structures with space groups R$\bar{3}$c (167), $I4/mcm$ (140), or $Imma$ (74) and the M_2^+ mode may freeze into $Im\bar{3}$ (204), $I4mmm$ (139), or $P4/mbm$ (127).[61] $Im\bar{3}$ and $I4mmm$ have 4 f.u./unit cell while the rest have 2 f.u./unit cell. Using SCAD with $L=4$ we relaxed AlF$_3$ in all six of these structures and find the energy is lowered from the cubic structure by 63, 18, 38, 44, 35, and 18 meV/f.u. for space-group numbers 167,

140, 74, 204, 139, and 127, respectively. Since the energy is lowered substantially more for R$\bar{3}$c than the rest, and it is known to be the low-temperature structure, the other structures are not considered further.

The SCAD energy changes for $L=2$ to $L=10$ are plotted as a function of distortion to the R$\bar{3}$c structure in Fig. 9. Lattice vectors are fixed by the cubic lattice with $a=a_0$. Similar curves for $L=11$ and $L=12$ lie between the $L=9$ and $L=10$ curves, very close to the $L=7$ curve. The energy is symmetric about the Wyckoff value 0.5 (0.75), which gives
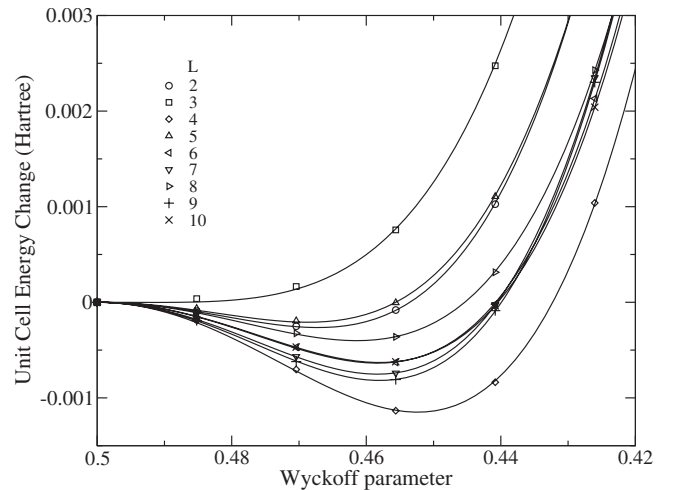
FIG. 9. SCAD results for energy change of 2 f.u. of AlF$_3$ from the cubic $a=a_0$ structure to the R$\bar{3}$c structure as a function of Wyckoff parameter.

TABLE II. Energy change (ΔU) and volume change (ΔV) of 2 f.u. of AlF_3 upon relaxing from the cubic structure (a_0) to $R\bar{3}c$, the e site Wyckoff parameter x, and both hexagonal (a and c) and rhombohedral (a_r and α_r) lattice parameters.

Method	a_0 (bohr)	ΔU (meV)	ΔV (bohr^3)	x	a (bohr)	c (bohr)	α_r (bohr)	α_r (deg)
$L=4$	6.762	126	45.6	0.412	9.214	23.372	9.434	58.47
$L=5$	6.775	34	28.3	0.433	9.351	23.518	9.518	58.84
$L=6$	6.767	70	40.8	0.417	9.254	23.419	9.460	58.57
$L=7$	6.758	71	34.7	0.424	9.268	23.493	9.485	58.50
KSLDA[a]	6.708	93	118.7	0.402	8.653	22.440	8.995	57.5
Expt.[b]				0.428	9.317	23.520	9.508	58.68

[a]From Ref. 67.
[b]From room-temperature x-ray data of Daniel *et al.* (Ref. 64).

the cubic structure in the hexagonal (rhombohedral) setting. The corresponding energy changes are about four times larger when the lattice is allowed to relax along with the Wyckoff parameter. These changes are shown in Table II.

Our results are in reasonably good agreement with the experimental room-temperature structure. The DFT results of Chen *et al.*[67] show a substantially larger lattice distortion, which lowers the energy by 6.5 times the cubic lattice result. This may be due to the fact the experiments were carried out at room temperature. Other KSLDA results[41] obtained using the LAPW method give $a_0=6.75$ bohr, somewhat higher than the value of Chen *et al.*[67]

We also calculated the phonon frequencies at Γ for the relaxed $R\bar{3}c$ structure for comparison with available experimental values and KS results (Table III). The SCAD results are reported, as in Table I, as the average of $L=4$ 5, 6, and 7 values. However, the contribution to the Γ^- mode frequencies from the nonregular part of the dynamical matrix is not included. We note that the SCAD result for the highest-frequency Raman-active mode is substantially (20%) too low.

VI. SILICON CARBIDE

The SCAD method is expected to work best for highly ionic compounds, such as fluorides, and we have seen that it

does rather well for AlF_3. On the other hand, silicon carbide has both elements in the same row of the periodic table, raising the question: Which way would the charge like to flow (if at all) to form an ionic bond?

First, we examine the energy as a function of charge transfer for various lattice parameters a in the $B3$ (sphalerite) structure in a range larger than the equilibrium value a_0. These results illustrate Janak's theorem and show the SCAD monopole charges for $a \sim a_0$ are Si^{+4} and C^{-4}. Next, we compare the electronic structure, a_0 and the bulk modulus B with results obtained from a KS band-structure calculation using the LAPW method. We then make similar comparisons for phonon frequencies, including the LO-TO splitting. Finally, we compare U for the $B3$ structure with that of the $B1$ and wurtzite structures.

In several places in this section SCAD results are compared with KS results. Unless otherwise stated, the KS results were derived using the full potential linearized augmented plane-wave (LAPW) method[68–70] with an RK_{max} value[71] of 8.5 and muffin-tin radii of 1.4 bohr for each atom; which produces ~ 225 plane waves per atom at the equilibrium volume. Both SCAD and LAPW calculations use the LDA of Hedin and Lundqvist[72] for exchange and correlation energies.

TABLE III. Frequencies (in cm^{-1}) for AlF_3 in the $R\bar{3}c$ structure at the Γ point of the Brillouin zone: from the SCAD and KSLDA (Ref. 67) calculations and room-temperature Raman (Ref. 64) measurements. Irreducible representation labels are those of ML (Ref. 66) with degeneracies in parentheses.

Γ^+				Γ^-	
ML	SCAD	KSLDA	Expt.	ML	SCAD
$1^+(1)$	180 ± 14	205	158	$1^-(1)$	246 ± 9
$2^+(1)$	340 ± 8	361		$1^-(1)$	516 ± 11
$2^+(1)$	688 ± 8	691		$2^-(1)$	283 ± 8
$3^+(2)$	109 ± 9	182	98	$2^-(1)$	560 ± 14
$3^+(2)$	358 ± 8	350	383	$3^-(2)$	209 ± 8
$3^+(2)$	384 ± 21	487	481	$3^-(2)$	296 ± 12
				$3^-(2)$	511 ± 12
				$3^-(2)$	573 ± 15
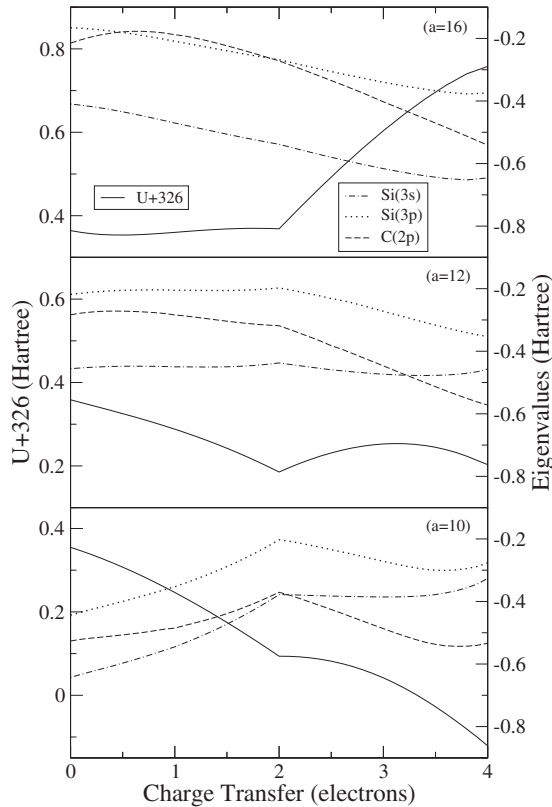
FIG. 10. Total energy U (left axis) and eigenvalue energies for the Si(3s), Si(3p) and C(2p) states (right axis) as a function of charge transfer from silicon to carbon in the $B3$ structure for three values of lattice parameter; $a=16$, 12, and 10 bohr for the top, middle, and bottom panels, respectively.

A. Charge transfer

Consider a silicon atom and a carbon atom isolated from each other. Each have two valence electrons, which we occupy equally among the Si(3p) and C(2p) states, respectively. The Si(3p) level is slightly higher in energy than the C(2p) level. We know from Janak's theorem[42] that U will be lowered by transferring some amount of electrons from the Si(3p) states to the C(2p) states. We find the minimum energy occurs when ~ 0.07 electrons are transferred, and, of course, the Si(3p) and C(2p) eigenvalues become equal at that value of charge transfer.

Results in Fig. 10 show that increasingly more charge must be transferred from silicon to carbon in the $B3$ structure as a is reduced in order to achieve the minimum U. For these calculations we use $L=6$ and $r_c=5$ to generate both silicon and carbon basis functions. The top panel ($a=16$) shows that the minimum energy is produced by a charge transfer of ~ 0.5 at the first point where the Si(3p) and C(2p) levels cross or become degenerate. The second crossing (degeneracy) corresponds to a maximum in U near ~ 1.9. The sharp increase in U for transfers >2 results from the fact that the Si(3p) electrons have all been transferred and additional transfer must come from the deeper Si(3s) levels. The middle panel ($a=12$) shows the minimum U with two electrons transferred is nearly the same as that with four electrons transferred. At the minimum for two electrons trans-
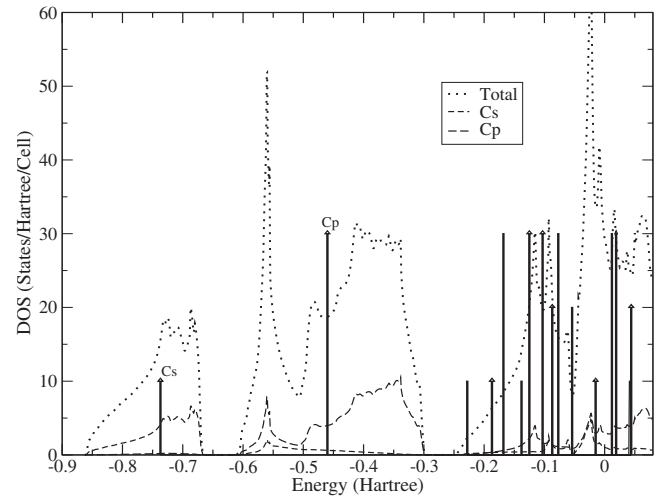
FIG. 11. Total DOS (dotted line), C(2s) partial DOS (short-dashed line), and C(2p) partial DOS (long-dashed line), computed by the KS-LAPW method for $a=8.2$ for comparison with SCAD eigenvalues for silicon (carbon), denoted by heavy solid lines without (with) arrow heads, and computed for $a=8.0$. Height of lines divided by 10 gives their degeneracy.

ferred U has a discontinuous slope, which, again, results from the fact that all of the Si(3p) electrons have been transferred and further transfer must come from the deeper Si(3s) levels. The maximum at ~ 3.2 corresponds to the crossing (degeneracy) of the Si(3s) and C(2p) levels. A further decrease in lattice parameter to $a=10$ moves this maximum along with the level crossing almost all the way to the two-electron-transferred value. For $a<10$ the energy decreases monotonically with charge transfer from zero to four electrons. For $a<12$, SCAD finds the lowest U results from complete charge transfer, producing Si^{+4} and C^{-4} ions.

When no charge is transferred from the atoms (left side of Fig. 10), U changes very little for $a>10$. This indicates the value of r_c used in the calculation was sufficiently large for convergence. Otherwise, if large r basis functions were needed, then there would be more substantial atomic overlap, causing a greater change in energy in the range $10<a<16$. On the other hand, there is a large change in energy in this range for the fully ionic configuration (right side of Fig. 10), owing a large change in the Madelung energy.

B. Electronic Structure

We have applied the KS-LAPW method to calculate the density of states (DOS) for comparison with the eigenvalues determined by SCAD, both determined for the $B3$ structure. Approximate equilibrium lattice parameters were used for both calculations, $a=8.2$ for KS and $a=8.0$ for SCAD. For this comparison we use the same SCAD basis employed to study charge transfer, namely, $L=6$ and $r_c=5$ for both silicon and carbon. The KS-derived DOS and the SCAD eigenvalues are plotted in Fig. 11. The DOS has been shifted so that the SCAD carbon 2s level is centered, approximately, in the corresponding band. The next higher C(2p) level also lies approximately in the center of the C$_p$ band. The next lowest

band occurs at −3.54 hartree, which compares with the Si(2p) SCAD derived value of −3.35 hartree. The C_s- and C_p-decomposed DOSs are based on muffin-tin radii of 1.65 bohr for both silicon and carbon and represent the largest contributions to the total DOS in those regions. The second largest contribution (not shown) in the C_s (C_p) region is seven (six) times smaller and has Si_s (Si_p) character. The character of the conduction band has silicon s, p, and d and carbon s, p, and d in relative amounts of 0.23, 0.44, and 0.20 and 0.30, 1.08, and 0.10, respectively. The LAPW band gap is 1.43 eV while the difference between highest occupied and lowest unoccupied SCAD levels is 6.3 eV. Of course, SCAD does not have bands, and hence, no well defined band gap. Nevertheless, we note that the SCAD C_s and C_p levels fall near the center of the corresponding LAPW bands, and higher SCAD levels fall in the LAPW conduction band. The SCAD levels in the conduction-band region can depend on the particular basis selected, even among bases that are well converged with respect to U. For example, we note that U converges for values of r_c for silicon that are quite small, ~1 bohr. However, using $r_c = 1$ for silicon removes most of the silicon levels from the conduction region. Since they are not occupied, it does not effect the value of U.

A convergence analysis for r_c similar to that shown in Sec. V A for AlF$_3$ was performed. Results show convergence for $r_c > 1.2$ bohr for the silicon basis, and about $r_c > 3.4$ bohr for the carbon basis. We increased these values by 0.8 to generate the results reported here. Changes produced by increasing $L > 2$ for silicon are very insignificant, owing to its tightly bound spherically shaped charge density. The cutoff radius (R_c) beyond which electrostatic contributions are included as point poles is selected to include 46 neighbors.

C. Cubic-structure results

The equation of state for the cubic ($B3$) structure of SiC computed using SCAD with increasing values of L for the carbon basis is compared with the KS result derived by the LAPW method in Fig. 12. The SCAD energy minimum converges to about 0.4 hartree above the KS value and a few percent smaller equilibrium volumes. Results for the equilibrium lattice parameter a_0 show a small peak in a_0 vs L at $L = 6$ with only small (less than 1%) changes for $L > 4$. Thus, for the remainder of this section we limit ourselves to results obtained using $L = 5$, 6, and 7.

Values for a_0, bulk modulus B, Born effective charge Z^*, and high-frequency dielectric constant ϵ_∞ are listed in Table IV. The major errors in the SCAD results are in the values for a_0, which are too small, and in the values for ϵ_∞, which are too large. Phonon frequencies in $B3$ SiC were obtained from SCAD energy differences using the FROZSL (Ref. 60) method described above for AlF$_3$. They are listed in Table V along with results from KS calculations and experiment. The splitting of the LO from the TO mode at Γ comes from the nonregular part of the dynamical matrix. In this case, the splitting is given by

$$\omega_{LO}^2 - \omega_{TO}^2 = \frac{4\pi Z^{*2} e^2}{V \mu \epsilon_\infty}, \qquad (49)$$

where V is the volume per unit cell, μ is the reduced mass, and e the electronic charge. We can test this result by com-
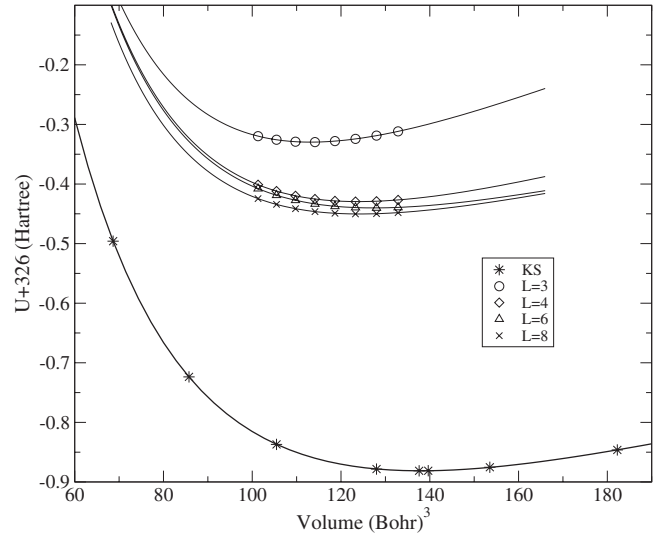
FIG. 12. Total energy U as a function of volume per primitive unit cell for SiC in the $B3$ structure, computed using the KS method and the SCAD method with increasing values for L in the carbon basis. The curves were obtained using a four-parameter Birch (Ref. 73) fit to the points as labeled.

puting phonon frequencies for wave vectors near but not exactly at $\mathbf{q} = 0$. For this test $L = 6$ energies for structural distortions provided by FROZSL with $\mathbf{q}$ in the $(1,1,1)$ direction are employed. This choice of wave vector direction provides further comparison with experimental results.

SCAD frequencies for wave vector q in the (111) (λ) direction are compared with available experimental results in Fig. 13. The agreement is generally quite good. The LO frequency at $q = 0$ was computed using calculated values for Z^* and ϵ_∞. Notice that this value connects smoothly to the rest of the LO branch, which, does not explicitly depend on Z^* and ϵ_∞.

D. Energy of other structures

In addition to the zinc-blende structure we have computed the energy of SiC in the wurtzite and rocksalt structures for

TABLE IV. Equilibrium lattice constant a_0, bulk modulus B, Born effective charge Z^*, and high-frequency dielectric constant ϵ_∞ for SiC in the $B3$ structure.

Method	a_0 (bohr)	B (Mbar)	Z^*	ϵ_∞
$L=5$	7.950	2.60	2.87	8.02
$L=6$	7.989	2.30	2.72	8.01
$L=7$	7.948	2.32	2.83	7.94
KS-LDA[a]	8.195	2.26		
KS-LDA[b]	8.239	2.10	2.72	6.97
Expt.[c]	8.239	2.24	2.70	6.52

[a]LAPW with Hedin-Lundqvist (Ref. 72) LDA.
[b]LAPW results of Wang *et al.* (Ref. 74) with Wigner (Ref. 75) LDA.
[c]From Wang *et al.* (Ref. 74) and references therein.

TABLE V. Phonon frequencies (in cm^{-1}) for SiC in the $B3$ structure at Γ, X, and L points of the Brillouin zone: SCAD results for selected values of L for comparison with KS and experimental results.

	Γ_{TO}	Γ_{LO}	X_{TA}	X_{LA}	X_{TO}	X_{LO}	L_{TA}	L_{LA}	L_{TO}	L_{LO}
$L=5$	825	1001	397	668	785	851	291	625	777	876
$L=6$	775	941	381	624	740	778	281	601	730	859
$L=7$	802	980	392	631	749	840	274	598	750	868
KS[a]	774	945	361	622	741	807	257	601	747	817
KS[b]	783	956	366	629	755	829	261	610	766	838
Expt.[c]	796	972	373	640	761	829	266	610	766	838

[a]LAPW results of Wang *et al.* (Ref. 74).
[b]Plane-wave pseudopotential method (Ref. 76).
[c]Based on Raman data of polytypes (Ref. 77).

comparison with KS derived energy differences for these structures. For both SCAD and KS there is only a small energy difference between that of the zinc-blende and wurtzite structures. However, SCAD favors the wurtzite structure by 15, 30, and 13 meV/f.u., respectively, for $L=5$, 6, and 7, while the LAPW-KS calculations of Bernstein *et al.*[78] favors the zinc-blende structure by ~5 meV. The energy of the rocksalt structure is much higher than the $B3$ or wurtzite values for both SCAD and KS. However, the values obtained differ significantly, ~2.6 eV for SCAD, and ~1.3 eV for KS.

VII. DISCUSSION

In this section we discuss the SCAD method, in general. Our remarks are based on the contents of this paper and on earlier published and unpublished results as well. SCAD is a density functional method that does not depend on any assumptions beyond the form of exchange, correlation, and kinetic-energy approximations employed. Results obtained so far make use of the Thomas-Fermi approximation to account for kinetic energy of overlapping densities, which is expected to be the greatest source of error.
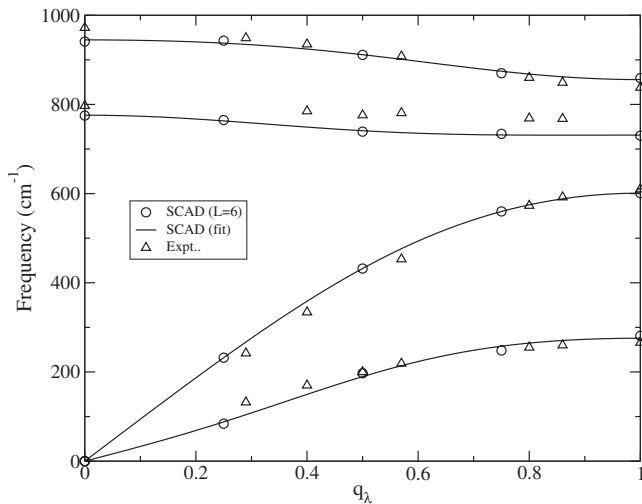
FIG. 13. Comparison of SCAD results for phonon frequencies with experimental values for wave vector q_λ along the (111) direction.

There are two fundamental convergence parameters governing the angular and radial variation of charge densities at each site, L and r_c. They are the maximum value of l used in the spherical harmonic part of basis functions at each site and r_c gives the radial extent of the bases. For any given L value, SCAD converges quickly with increasing r_c. In principle, converged values of r_c could depend on L or *vice versa*, but we have not observed this to be the case. Convergence with respect to L can be difficult if L_v, the maximum l in the potential, is not constrained by satisfaction of the Schrödinger equation. A satisfactory method to accomplish this, discussed in detail in Sec IIIB, limits the value of L_v to that of L. With this method, we believe acceptable convergence for most systems can be achieved for L in the range of 4–6. We have not observed significant benefits from using much higher L values, except for special cases, such as the water molecule, that have no overlap kinetic energy. This suggests that higher-order expansions for kinetic-energy functionals will be needed to achieve significant improvement in accuracy by using much higher L values.

While SCAD is most reliable for ionically bonded systems it does rather well for many systems, which are usually considered to have large amounts of covalent bonding. This is true for SiC, for which results are presented in detail above. Bonding charge between ions in SiC is usually considered to be a covalent effect, resulting from a linear combination of orbitals on neighboring sites. In the SCAD method the monopole charges are found to be Si^{+4} and C^{-4} with bonding charge resulting from nonspherical distortions of the C^{-4} ions. Because the monopole charges are well defined and fixed by the SCAD method, a straightforward calculation of polarization and related quantities is permitted.[39]

We find that SCAD errors, or, by implication, errors due to the use of the Thomas-Fermi approximation, are significantly greater when charge-density overlap involves d-level valence electrons. For example, when d electrons are not present as valence states, as is the case for alkali halides, lattice parameters are predicted fairly accurately, typically a few percent too small.[35] On the other hand, the lattice parameter for AgCl is too large by about 15%. It is a general trend that equilibrium volumes are predicted substantially too large when d electrons occupy valence states.

Another trend in SCAD errors can be seen by comparing the relative energies of a compound in various crystal struc-

tures with KS results. Specifically, distortions to lower symmetry structures tend to have energies too low compared to the higher symmetry structures. For example, we have seen that the SiC wurtzite structure is overstabilized compared to the zinc-blende structure and both are overstabilized compared to that of the rocksalt structure. Another example is MgO, where SCAD produces rock salt and zinc-blende energies that are nearly degenerate, whereas the KS result has rock salt energy lower by about 0.1 eV/atom.

Other examples showing this trend (too low energy for lower symmetry structures) are compounds that have distorted perovskite structures—SCAD tends to overestimate the size of instabilities involved in such distortions. In particular, results for $SrTiO_3$ show a highly unstable ferroelectric mode. In reality, the ferroelectric mode should be soft, but stable, while an unstable zone-boundary mode produces the observed transition to a distorted perovskite at low temperature. In this case, the unstable ferroelectric mode can be stabilized with good overall agreement with experiment by simply scaling the Thomas-Fermi energy by a factor of ~ 1.04, enough to achieve the correct equilibrium volume.[27]

Results for $BaTiO_3$ show a similar problem. Specifically, SCAD predicts a ferroelectric instability in $BaTiO_3$ that is too large, unless the Thomas-Fermi energy is scaled similarly to the calculations for $SrTiO_3$. Ironically, the SCAD model, which has fully ionic monopole charges, tends to exaggerate ferroelectric instabilities, while the KS model suggests a covalent bonding picture is required to produce ferroelectric instability.[79] This apparent contradiction stems from the fact that two different methods (SCAD and KS) are used to represent the total charge density. Predicting the correct size of the ferroelectric instability is a challenging problem for the KS model[80,81] as well as SCAD. As mentioned, some improvement in SCAD results simply from scaling the Thomas-Fermi form to achieve the correct equilibrium volume. Of course, a more satisfactory solution would be to use a better kinetic-energy functional at the outset. This is perhaps the most important task for future development of the SCAD method.

Some important systems are even more problematic for SCAD in its present form. Silicon is a good example. If we force the two silicon atoms (diamond structure) to be equivalent by symmetry constraints and occupy the three degenerate p levels equally, then we obtain a reasonable value for cohesive energy, ~ 5.5 eV/atom (experimental value of ~ 4.6). However, other properties, such as phonon frequencies are seriously wrong. Moreover, if the atoms are not constrained to be equivalent by symmetry, then the cohesive energy is approximately doubled, either by allowing four electrons to transfer from one atom to another, creating Si^{+4} and Si^{-4}, or by allowing the neutral atoms to distort to a symmetry lower than that of diamond. In either case, the results obtained for phonon frequencies have large errors. Surprisingly, the $Si^{+4}Si^{-4}$ ionic picture does not produce large errors for the splitting of the longitudinal and transverse optical mode frequencies, which, of course, is zero for silicon. As long as L is sufficiently large when the ion sublattices are displaced, the negative ions deform with large enough dipole moments to approximately cancel the contribution from displaced monopoles, causing a nearly zero

value for Z^*. We suspect that silicon puts a greater demand on the approximation for overlap kinetic energy than ionic systems and speculate that, given a more accurate kinetic-energy functional, these different pictures for silicon would produce essentially the same results for total charge density and energy.

With caution, SCAD can be applied to metals. For CaV_4O_9, the highest occupied level of the system is the lowest $3d$ level of V and it is occupied by a single electron.[82] Having the Fermi energy at a half occupied level suggests metallic-like conductivity. A more troublesome example is sodium. We find SCAD yields the transfer of an electron to produce Na^{+1} and Na^{-1} ions. This was noted using an earlier version of the SCAD approach.[26] While this picture could well change with the use of more accurate kinetic-energy functionals, nevertheless, we obtain reasonably accurate results for lattice parameter, bulk modulus, and cohesive energy with the ionic picture. Assuming the bcc (CsCl) structure and using $L=4$, we find 7.97(8.09) bohr, 0.076(0.064) Mbar, and 1.18(0.93) eV/atom, where experimental quantities are shown in parentheses. The highest occupied level ($3s$ of Na^{-1}) is about 1 eV lower than the lowest unoccupied level ($3s$ of Na^{+1}), and the energy barrier for transfer of charge between the two sublattices is 0.5 eV. Phonon frequencies are about the right magnitude for most zone-boundary modes, but the mode at Γ (H in the Brillouin zone of the bcc lattice) shows a small instability, lowering the energy from that of the undistorted structure by ~ 1 meV.

If we compute the dielectric susceptibility for this ionic sodium model, we find something unusual. For all insulating systems we have tried thus far, including the SCAD Si^{+4} and Si^{-4} ionic pictures of silicon, we were able to compute a value for dielectric susceptibility by numerically evaluating $\Delta P / \Delta E$ because P is found to be a linear function of E for small E. On the other hand, a different behavior is seen for $Na^{+1}Na^{-1}$. Specifically, we find $P \propto E^\gamma$, where $0 < \gamma < 1$. This produces a divergent value for $\Delta P / \Delta E$ in the limit of small E, consistent with that expected for a conductor.

Notwithstanding the problematic examples cited above, we note that SCAD can be expected to give reasonably accurate results many insulating systems with varying degrees of ionic bonding character. For such systems SCAD may be able to handle complex systems with defects and surfaces that would be difficult to treat with KS DFT methods.

ACKNOWLEDGMENTS

APPENDIX A: KINETIC ENERGY FUNCTIONALS

Lacks and Gordon[83] proposed nonlocal corrections to the Thomas-Fermi[84,85] kinetic-energy functional that have the

form of generalized exchange-correlation functionals for the exchange-correlation energy. Thus in their approximation, the kinetic energy of an electron gas with density $n(\mathbf{r})$ is given by

$$T[n(\mathbf{r})] = A_k \int d\mathbf{r} \, n(\mathbf{r})^{5/3} F[s(\mathbf{r})], \tag{A1}$$

where for an unpolarized electron gas

$$A_k = \pi^{4/3} 3^{5/3}/10 \tag{A2}$$

if the energy is in hartrees, and $s(\mathbf{r})$ is a measure of the local nonuniformity of the electron gas,

$$s(\mathbf{r}) = \frac{|\nabla n(\mathbf{r})|}{2n(\mathbf{r})k_f(\mathbf{r})}. \tag{A3}$$

In the case of the uniform electron gas, $s(\mathbf{r}) = 0$ everywhere, and Eq. (A1) reduces to the Thomas-Fermi kinetic energy if $F[0] = 1$. We have also examined nonlocal functionals of the form of a scaled Thomas-Fermi kinetic energy plus a scaled Weizsäcker[86] kinetic energy,

$$T_k = kT_{\mathrm{TF}} + \tau \int d^3r \frac{|\nabla n(\mathbf{r})|^2}{n(\mathbf{r})}, \tag{A4}$$

where T_{TF} is the Thomas-Fermi kinetic energy. This can be shown to reduce to the form Eq. (A1) if we set

$$F[s(\mathbf{r})] = k + \frac{40}{3}\tau s(\mathbf{r})^2 \tag{A5}$$

Lacks and Gordon[20] considered only those functions $F[s]$ which are even in s, so we define a new quantity,

$$\sigma(\mathbf{r}) = s(\mathbf{r})^2 = \frac{|\nabla n(\mathbf{r})|^2}{4n(\mathbf{r})^2 k_f(\mathbf{r})^2}. \tag{A6}$$

Since $k_f \propto n^{1/3}$ we can take

$$\sigma(\mathbf{r}) = \alpha n(\mathbf{r})^{-8/3} |\nabla n(\mathbf{r})|^2, \tag{A7}$$

where

$$\alpha = (24\pi^2)^{-2/3}. \tag{A8}$$

Then, writing $F[\sigma]$ in place of $F[s]$, we have

$$T[n(\mathbf{r})] = A_k \int d^3r \, n(\mathbf{r})^{5/3} F[\sigma(\mathbf{r})]. \tag{A9}$$

Our task is to determine the Kohn-Sham "potential" arising from Eq. (A9).

We wish to study the change $T[n] \rightarrow T[n] + \delta T[n]$ as we make the change $n \rightarrow n + \delta n$. Keeping only the terms linear in δn, we have

$$\delta T[n(\mathbf{r})] = A_k \int d^3r \, n(\mathbf{r})^{2/3} \left\{ \frac{5}{3} F[\sigma(\mathbf{r})]\delta n(\mathbf{r}) \right. $$
$$\left. + n(\mathbf{r})F'[\sigma(\mathbf{r})]\delta\sigma(\mathbf{r}) \right\} + O[(\delta n)^2], \tag{A10}$$

where $\delta\sigma$ is the change in σ as $n \rightarrow n + \delta n$,

$$\delta\sigma(\mathbf{r}) = -\frac{8}{3}\frac{\sigma(\mathbf{r})}{n(\mathbf{r})}\delta n(\mathbf{r}) + 2\alpha n(\mathbf{r})^{-8/3} \nabla n(\mathbf{r}) \cdot \nabla \delta n(\mathbf{r})$$
$$+ O[(\delta n)^2]. \tag{A11}$$

Substituting Eq. (A11) into Eq. (A10) and separating the integrals containing δn and $\nabla \delta n$, we find

$$\delta T[n(\mathbf{r})] = \frac{1}{3}A_k \int d^3r \, n(\mathbf{r})^{2/3}\{5F[\sigma(\mathbf{r})]$$
$$- 8\sigma(\mathbf{r})F'[\sigma(\mathbf{r})]\}\delta n(\mathbf{r})$$
$$+ 2\alpha A_k \int d^3r \frac{F'[\sigma(\mathbf{r})] \nabla n(\mathbf{r})}{n(\mathbf{r})} \cdot \nabla \delta n(\mathbf{r}). \tag{A12}$$

Applying the divergence theorem to the third line of Eq. (A12) and noting that integrals over the boundary of a periodically repeated unit cell vanish, we find

$$\delta T[n(\mathbf{r})] = \frac{1}{3}A_k \int d^3r \, n(\mathbf{r})^{2/3}\{5F[\sigma(\mathbf{r})]$$
$$- 8\sigma(\mathbf{r})F'[\sigma(\mathbf{r})]\}\delta n(\mathbf{r})$$
$$+ A_k \int d^3r \, 2\alpha \frac{|\nabla n(\mathbf{r})|^2}{n(\mathbf{r})^2}F'[\sigma(\mathbf{r})]\delta n(\mathbf{r})$$
$$- 2\alpha A_k \int d^3r \left\{ F'[\sigma(\mathbf{r})]\frac{\nabla^2 n(\mathbf{r})}{n(\mathbf{r})} \right. $$
$$\left. + F''[\sigma(\mathbf{r})]\frac{\nabla n(\mathbf{r}) \cdot \nabla \sigma(\mathbf{r})}{n(\mathbf{r})} \right\} \delta n(\mathbf{r}). \tag{A13}$$

Using Eq. (A7) on the third line of Eq. (A13), we obtain the final expression as

$$\delta T[n(\mathbf{r})] = A_k \int d^3r \, \delta n(\mathbf{r}) \left(\frac{1}{3}n(\mathbf{r})^{2/3}\{5F[\sigma(\mathbf{r})] \right.$$
$$- 2\sigma(\mathbf{r})F'[\sigma(\mathbf{r})]\}) - 2\alpha F'[\sigma(\mathbf{r})]\frac{\nabla^2 n(\mathbf{r})}{n(\mathbf{r})}$$
$$\left. - 2\alpha F''[\sigma(\mathbf{r})]\frac{\nabla n(\mathbf{r}) \cdot \nabla \sigma(\mathbf{r})}{n(\mathbf{r})} \right). \tag{A14}$$

The Kohn-Sham potential is related to its functional by the functional derivative,

$$v_T(\mathbf{r}) = \frac{\delta T[n(\mathbf{r})]}{\delta n(\mathbf{r})}, \tag{A15}$$

so from Eq. (A14) we find

$$v_T(\mathbf{r}) = (A_k n(\mathbf{r})^{2/3}\{5F[\sigma(\mathbf{r})] - 2\sigma(\mathbf{r})F'[\sigma(\mathbf{r})]\})/3$$
$$- 2\alpha\{F'[\sigma(\mathbf{r})]\nabla^2 n(\mathbf{r})$$
$$+ F''[\sigma(\mathbf{r})] \nabla n(\mathbf{r}) \cdot \nabla\sigma(\mathbf{r})\}/n(\mathbf{r})). \tag{A16}$$

APPENDIX B: INTEGRATION AND INTERPOLATION

Radial functions are stored on a logarithmic mesh chosen so that the *interval* between points increases exponentially. Specifically, the nth interval is given by

$$r_{n+1} - r_n = r_1(1 + g)^n, \tag{B1}$$

where the value of r_1 is selected to be the first nonzero mesh point ($r_0 = 0$) and g is a selected growth factor. Clearly, smaller atoms can have a larger value for r_1 than larger ones, and this, in turn, is related to the maximum value of β in the tabulated[43,44] Slater functions, which is approximately the atomic number. We find that $g \sim 1/50$ with $r_1 = g/(2\beta_{max})$ gives a few hundred dense radial mesh points with $r < 50$ while $g \sim 1/6$ with $r_1 \sim 1/20$ gives a few tens of course radial mesh points with $r < 50$, which, together, permit numerical accuracy in total energy to $\sim 0.000\,001$ hartree. Precision in the calculation of forces can be improved by starting r_1 closer to the nucleus, say, $r_1 = g/(2S_F\beta_{max})$, where $S_F \sim 10$.

Equation (B1) implies

$$r_n = [(1 + g)^n - 1]\frac{r_1}{g}. \tag{B2}$$

The derivative of r with respect to n,

$$r_n' = \ln(1 + g)(1 + g)^n\frac{r_1}{g}, \tag{B3}$$

is used to facilitate radial integrations. The usual quadrature weights (assuming r is just a constant times n) are simply multiplied by r_n'. For improved accuracy in the $l = 0$ part of the Hartree potential the SCAD program can include a selected number N_{cp} of Gaussian points between the radial mesh points.

The integration of a smooth function of r times one with a discontinuity in its radial derivative must be treated carefully. In the SCAD method, discontinuities appear in the radial derivatives of the potential at values of r corresponding to the positions of neighboring atoms. This results from the lower limit of the Löwdin integrals in Eq. (D9) and from the $r_<^l/r_>^{l+1}$ factor in the addition theorem which is used to incorporate the potential from neighboring nuclei. These sharp features in the potential can produce noise in the total energy as a function of structural distortions if integrations are carried out by straightforward quadrature on a fixed radial mesh. We handle this problem by a procedure which retains points on a fixed radial mesh and includes extra points that vary with structural distortions. As the total potential for a given atom is accumulated on the fixed mesh, we omit contributions from Löwdin and neighboring nuclei for a selected number of points N_{np} on either side of the corresponding neighbor distances. Then, for each neighbor j, the Löwdin plus neighboring nuclei potential is evaluated at radii given by N_{gp} Gaussian quadrature points from the beginning of the omitted region to R_j and from R_j to the end of the omitted region. Only a few Gaussian points are needed for accurate integration on either side of R_j. Typically, 30–50 neighbors are needed for convergence, so a total of about two hundred extra points are needed to handle the integrations over the sharp features in the potential. This is a small part of the overall calculation.

Numerical integrations over solid angles (Ω quadrature) use directions and weights generated similarly to those of Gaussian quadrature, except that the generating functions are, in this case, spherical harmonics.[51] We find that about

$N_\Omega = 150$ quadrature directions are needed to produce satisfactory accuracy in the SCAD method. As mentioned in Sec. III A the most computationally intensive part of the calculation is in determining the smooth part of the potential, v_s. This requires evaluation of the densities and nonspherical parts of electrostatic potentials due to neighbors at each point on the course mesh. Typically, an atom may overlap with about 40 neighbors and the course mesh may have ~ 30 radial points for ~ 150 directions. Assuming radial functions are required up to $l = 4$, this gives a total of over 2×10^6 ($2 \times 15 \times 40 \times 30 \times 150$) interpolations per atom. We use a cubic spline interpolation with our indices taken to be the independent variable. This minimizes the number of operations in each interpolation without any loss of accuracy.

APPENDIX C: DISTANT POLE POTENTIAL

The potential v_p, due to atoms outside the cutoff radius R_c, is given by the electrostatic potentials of point poles centered at the atomic sites and is separated into long- and short-ranged parts,

$$v_p = v_{lr} + v_{sr}. \tag{C1}$$

The long-ranged part, v_{lr}, comes from $l \leq 2$ poles and is obtained with the help of Ewald's method. The short-ranged contribution, v_{sr} results from $l \geq 3$ and is determined by straightforward real-space summations. First, consider the long-ranged contribution.

Ewald's method provides a rapidly convergent formula for the potential of a lattice of point charges in a uniform compensating background. A good discussion of the method is given by Slater.[87] The method employs linear superposition of two oppositely charged, but otherwise identical, Gaussian densities centered at the sites of the point charges. The negative Gaussian densities combine with the positive point charges to give a rapidly convergent real-space sum for their contribution to the potential and the positive Gaussian densities combine with the negative background to give a rapidly convergent Fourier series expansion for their contribution. The potential at $\mathbf{r}$ due to unit point charges at $\mathbf{x}(l) + \mathbf{r}'$, where $\mathbf{x}(l)$ are lattice vectors, in a uniform background is given by

$$v_m(\mathbf{r}, \mathbf{r}') = \frac{4\pi}{V}\sum_{\mathbf{Q}}' \frac{e^{-(Q^2/4\epsilon)}}{Q^2}e^{i\mathbf{Q}\cdot(\mathbf{r}-\mathbf{r}')}$$
$$+ \sum_l \frac{erfc(|\mathbf{x}(l) + \mathbf{r} - \mathbf{r}'|)\epsilon}{|\mathbf{x}(l) + \mathbf{r} - \mathbf{r}'|} - \frac{\pi}{V\epsilon^2}, \tag{C2}$$

where $\mathbf{Q}$ are reciprocal-lattice vectors, the prime on the summation over $\mathbf{Q}$ indicates the $\mathbf{Q} = 0$ term is omitted, and erfc, the complimentary error function, is given by

$$\text{erfc}(x) = \frac{2}{\sqrt{\pi}}\int_x^\infty e^{-y^2}dy, \tag{C3}$$

and the last term is a constant of integration needed to make the result independent of the Gaussian parameter ϵ. The value of ϵ can be adjusted to give rapid convergence for both real and reciprocal space sums.

We put the point charges a displacement $\mathbf{r}'$ from the lattice vectors for convenience in deriving expressions for the potential due to point dipoles and quadrupoles. For example, we can place point charges of $\pm q$ at $\mathbf{r}' = \pm \hat{\mathbf{x}} d/2$. The resultant potential at $\mathbf{r}$ is given by $v_m(\mathbf{r}, \hat{\mathbf{x}} d/2) - v_m(\mathbf{r}, -\hat{\mathbf{x}} d/2)$. For small d the lowest-order (linear) term in an expansion of the above expression about $\mathbf{r}' = 0$ is the potential due to a lattice of point dipoles. In particular, we find the potential due to a lattice of point dipoles in the α direction is given by

$$v_{d_\alpha}(\mathbf{r}) = \frac{4\pi}{V} \sum_{\mathbf{Q}}' \frac{e^{-(Q^2/4\epsilon)}}{Q^2} \sin(\mathbf{Q} \cdot \mathbf{r}) Q_\alpha$$
$$+ \sum_l \left(\frac{4\epsilon}{\sqrt{\pi} r^2} e^{-r^2 \epsilon^2} + \frac{erfc(r\epsilon)}{r^3} \right) r_\alpha. \quad (C4)$$

Similarly, the potential due to point quadrupoles is given by the second-order term in the expansion of v_m about $\mathbf{r}' = 0$. We obtain

$$v_{q_{\alpha\beta}}(\mathbf{r}) = -\frac{2\pi}{V} \sum_{\mathbf{Q}}' \frac{e^{-(Q^2/4\epsilon)}}{Q^2} \cos(\mathbf{Q} \cdot \mathbf{r}) Q_\alpha Q_\beta$$
$$+ \frac{r_\alpha r_\beta}{2} \sum_l \left\{ \frac{2\epsilon}{\sqrt{\pi}} \left(\frac{2\epsilon^2}{r^2} + \frac{3}{r^4} \right) e^{-r^2\epsilon^2} + \frac{3 erfc(\epsilon r)}{r^3} \right\}$$
$$- \frac{\delta_{\alpha\beta}}{2} \sum_l \left\{ \frac{2\epsilon}{\sqrt{\pi} r^2} e^{-r^2\epsilon^2} + \frac{erfc(\epsilon r)}{r^3} \right\}. \quad (C5)$$

Calculations using these expressions for v_d and v_q have been tested against Eq. (C2) by modeling collections of point charges that approximate point dipoles and quadrupoles.

For the SCAD calculation we require spherical harmonic expansions of the potentials due to point poles that lie outside the cutoff radius R_c. Thus we must remove, from v_m, v_d, and v_q, the contributions from nearby poles with $\mathbf{x}(l) < R_c$. Specifically, these contributions are $1/s$ for monopoles, s_α/s^3 for dipoles, and $(3 s_\alpha s_\beta - \delta_{\alpha\beta} s^2)/2 s^5$ for quadrupoles, where $\mathbf{s}$ denotes the separation vector from $\mathbf{x}(l)$ to $\mathbf{r}$. Values for v_m, v_d, and v_q, with contributions from nearby poles removed, are determined on an angular grid for some selected value of $r = r_s$. The coefficients of the spherical harmonic expansion are then determined by numerical integration over the surface of the sphere with radius r_s (Appendix B, Ω quadrature). The radial dependence of v_d and v_q are solutions of Laplace's equation, in our case the r^l solutions. The radial dependence of the monopole potential v_m contains, additionally, a spherically symmetric term $\propto r^2$ that originates from the constant charge background. We remove this contribution before determining the spherical harmonic expansion of v_m. Of course, it necessarily sums to zero when the contributions from all the atoms in the crystal are included. In any case, the coefficients of the various spherical harmonic expansions of point-pole potentials need only be determined for one value of r_s. We find no significant variation in U over a wide range of values less that $\sim R_c/2$, and a good choice is $r_s \sim 1$ or 2.

In each iteration the point-pole spherical harmonic expansion coefficients are multiplied by the corresponding computed moments and summed over all atoms in the unit cell to give $v_{lr}^{(i)}$. Specifically,

$$v_{lr}^{(i;l,m)}(r) = r(l) \sum_{j,k} c(j,k) v_{pp}^{(l,m)}(j,i,k), \quad (C6)$$

where the j index designates $v_{pp} = v_m$, v_{d_1}, v_{d_2}, v_{d_3}, $v_{q_{11}}$, $v_{q_{21}}$, $v_{q_{22}}$, $v_{q_{31}}$, $v_{q_{32}}$, and $v_{q_{33}}$ for $j = 1, \ldots, 10$ respectively, the k index sums over all the atoms in the unit cell and the $c(j,k)$ are given by the multipole moments of each atom k and constants which transform between the Cartesian and spherical harmonic description,

$$c(1,k) = \frac{G_{0,0}^{(k)}(\infty)}{2\sqrt{\pi}} - Z_k, \quad (C7)$$

$$c(2,k) = -\Re[G_{1,1}^{(k)}(\infty)]\sqrt{8\pi/3}, \quad (C8)$$

$$c(3,k) = \Im[G_{1,1}^{(k)}(\infty)]\sqrt{8\pi/3}, \quad (C9)$$

$$c(4,k) = G_{1,0}^{(k)}(\infty)\sqrt{4\pi/3}, \quad (C10)$$

$$c(5,k) = \Re[G_{2,2}^{(k)}(\infty)]\sqrt{8\pi/15} - G_{2,0}^{(k)}(\infty)\sqrt{4\pi/45}, \quad (C11)$$

$$c(6,k) = -\Im[G_{2,2}^{(k)}(\infty)]\sqrt{32\pi/15}, \quad (C12)$$

$$c(7,k) = -\Re[G_{2,2}^{(k)}(\infty)]\sqrt{8\pi/15} - G_{2,0}^{(k)}(\infty)\sqrt{4\pi/45}, \quad (C13)$$

$$c(8,k) = -\Re[G_{2,1}^{(k)}(\infty)]\sqrt{32\pi/15}, \quad (C14)$$

$$c(9,k) = \Im[G_{2,1}^{(k)}(\infty)]\sqrt{32\pi/15}, \quad (C15)$$

$$c(10,k) = G_{2,0}^{(k)}(\infty)\sqrt{16\pi/5}, \quad (C16)$$

where G_{lm} is given in Eq. (14) and $r(l) = r^l$ for $r < R_c$. As r increases beyond R_c the radial dependence of the potential due to individual poles changes from r^l to $1/r^{l+1}$. We do not include this detail in the SCAD code because it does not affect results as long as R_c is sufficiently larger than the orbital cutoff radius r_c, a condition for convergence. Instead, we approximate this change in radial dependence by writing $r(l) = R_c^{2l+1}/r^{l+1}$ for $r > R_c$, which maintains continuity at R_c and gives a better representation of the radial dependence of the potential beyond R_c.

The potential due to $l \geq 3$ poles takes the same form as Eq. (C6),

$$v_{sr}^{(i;l,m)}(r) = r(l) \sum_{j,k} c(j,k) v_{pp}^{(l,m)}(j,i,k), \quad (C17)$$

except the coefficients v_{pp} are determined with real-space sums over poles at sites beyond R_c. Here the j index denotes the type of pole and whether it is purely real (odd j) or imaginary (even j). For example, let j denote the real part of a (l_j, m_j) pole. Then $v_{pp}^{(l,m)}(j,i,k)$ is the spherical harmonic expansion coefficient due to the kth lattice of (l_j, m_j) poles (with unit real part and zero imaginary part) excluding those within R_c of the ith site. Its value is obtained, like those for v_{lr}, by numerical integration over Y_{lm}^* times the potential on an angular grid for a selected radius r_s. Once these coeffi-

cients are determined they are multiplied by the true values of the j-type poles of k-type atoms $[c(j,k) = \Re G_{l_j,m_j}^{(k)}(\infty)$ for odd j and $c(j,k) = \Im G_{l_j,m_j}^{(k)}(\infty)$ for even $j]$ and summed over all j and k. The time required to determine values of v_{pp} for v_{sr} can be substantial because the lattice sums converge rather slowly for $l = 3$ poles and may require a few thousand terms to achieve total-energy results to a precision of 0.000 001 Hartree. Nevertheless, it is much more efficient to obtain this level of numerical accuracy using the point-pole strategy than could be achieved by simply increasing the value of R_c.

APPENDIX D: LÖWDIN TRANSFORMATION

Given a function expressed as a spherical harmonic expansion, the method for transforming that function to a spherical harmonic expansion about a new origin is known as Löwdin's α expansion. Following the treatment of Fletcher,[88] we expand a spherically symmetric function, $F(r') = f(r')Y_{0,0}$, in terms of spherical harmonics about a new origin. Here the "prime" is used to denote coordinates with respect to the "old" origin. The two origins are separated a distance a along the z axis. In this case, the spherical harmonic expansion about the new origin can be written as

$$F(\mathbf{r}) = \sum_l g_l(r)Y_{l,0}(\hat{\mathbf{r}}), \tag{D1}$$

where

$$g_l(r) = \sqrt{2l+1} \int_0^\pi f(r')P_l(\cos\theta)\sin(\theta)d\theta \tag{D2}$$

and θ is the polar angle. Expressing the integration in terms of the variable r', where $r'^2 = r^2 + a^2 - 2ar\cos(\theta)$, gives

$$g_l(r) = \frac{\sqrt{2l+1}}{ar} \int_{|a-r|}^{a+r} f(r')P_l\left(\frac{r^2 + a^2 - r'^2}{2ar}\right)r'dr'. \tag{D3}$$

For $l \leq 4$ we find

$$g_0(r) = d_0(r)I_0(r), \tag{D4}$$

$$g_1(r) = d_1(r)[-I_1(r) + (r^2 + a^2)I_0(r)], \tag{D5}$$

$$g_2(r) = d_2(r)\left[\frac{3}{2}I_2(r) - 3(r^2 + a^2)I_1(r) + \frac{1}{2}(3r^4 + 2r^2a^2 + 3a^4)I_0(r)\right], \tag{D6}$$

$$g_3(r) = d_3(r)\left[-\frac{5}{2}I_3(r) + \frac{15}{2}(r^2 + a^2)I_2(r) - \frac{1}{2}(15r^4 + 18r^2a^2 + 15a^4)I_1(r) + \frac{1}{2}(5r^6 + 3r^4a^2 + 3r^2a^4 + 5a^6)I_0(r)\right], \tag{D7}$$

$$g_4(r) = d_4(r)\left[\frac{35}{8}I_4(r) - \frac{35}{2}(r^2 + a^2)I_3(r) + \frac{15}{4}(7r^4 + 10r^2a^2 + 7a^4)I_2(r) - \frac{5}{2}(7r^6 + 9r^4a^2 + 9r^2a^4 + 7a^6)I_1(r)\frac{1}{8} \times (35r^8 + 20r^6a^2 + 18r^4a^4 + 20r^2a^6 + 35a^8)I_0(r)\right], \tag{D8}$$

$$I_l(r) = \int_{|a-r|}^{r+a} f(x)x^{2l+1}dx, \tag{D9}$$

and

$$d_l(r) = \frac{\sqrt{2l+1}}{(2ar)^{l+1}}. \tag{D10}$$

This is an efficient form for g_l because the integrals can be obtained by interpolating from tabulated values of the integral with limits from zero to the radial mesh values. However, for small r this expression for g_l becomes numerically unstable, owing to large cancellations that counter the effect of having r^{l+1} in the denominator of d_l. A way around this problem is to expand f in a Taylor series about a. The integrals,

$$I_l(r) = \int_{a-r}^{a+r} \sum_n \frac{f^{(n)}}{n!}(x-a)^n x^{2l+1}dx, \tag{D11}$$

where $f^{(n)}$ denotes the nth derivative of f evaluated at a, can then be performed analytically, the resultant polynomials substituted into the corresponding expressions for g_l and each term with some power of r in the denominator has an expression in its numerator that sums identically to zero. We obtain, after considerable algebra, the following expressions for g_l when f is expanded to fourth order:

$$g_0(r) = f^{(0)} + \frac{r^2}{3a}f^{(1)} + \frac{r^2}{6}f^{(2)} + \frac{r^4}{30a}f^{(3)} + \frac{r^4}{120}f^{(4)}, \tag{D12}$$

$$g_1(r) = \sqrt{3}\left[\left(\frac{r^3}{15a^2} - \frac{r}{3}\right)f^{(1)} - \frac{r^3}{15a}f^{(2)} + \left(\frac{r^5}{210a^2} - \frac{r^3}{30}\right)f^{(3)} - \frac{r^5}{210a}f^{(4)}\right], \tag{D13}$$

$$g_2(r) = \sqrt{5}\left[\left(\frac{r^4}{35a^3} - \frac{r^2}{15a}\right)f^{(1)} - \left(\frac{r^4}{35a^2} - \frac{r^2}{15}\right)f^{(2)} + \left(\frac{r^6}{630a^3} + \frac{r^4}{210a}\right)f^{(3)} - \left(\frac{r^6}{630a^2} - \frac{r^4}{210}\right)f^{(4)}\right], \tag{D14}$$

$$g_3(r) = \sqrt{7}\left[\left(\frac{r^5}{63a^4} - \frac{r^3}{35a^2}\right)f^{(1)} - \left(\frac{r^5}{63a^3} - \frac{r^3}{35a}\right)f^{(2)}\right.$$
$$+ \left(\frac{r^7}{1386a^4} + \frac{r^5}{210a^2} - \frac{r^3}{105}\right)f^{(3)}$$
$$\left. - \left(\frac{r^7}{1386a^3} - \frac{r^5}{1890a}\right)f^{(4)}\right], \tag{D15}$$

$$g_4(r) = \sqrt{9}\left[\left(\frac{r^6}{99a^5} - \frac{r^4}{63a^3}\right)f^{(1)} - \left(\frac{r^6}{99a^4} - \frac{r^4}{63a^2}\right)f^{(2)}\right.$$
$$+ \left(\frac{r^8}{2574a^5} + \frac{5r^6}{1386a^3} - \frac{2r^4}{315a}\right)f^{(3)}$$
$$\left. - \left(\frac{r^8}{2574a^4} + \frac{r^6}{4158a^2} - \frac{r^4}{945}\right)f^{(4)}\right]. \tag{D16}$$

Analogous expressions for $12 \geq l \geq 5$ and eight order in the Taylor expansion [Eq. (D11)] were derived and coded with the help of the MATHEMATICA software package.[89]

The small-r expansion is used for $r < 1.1r_l(a)$ and the large-r expansion is used for $r > 1.2r_l(a)$, where $r_l(a)$ is determined from the onset of noise in the large-r values with decreasing r. We find the onset of noise is quite abrupt, and for $1.1r_l(a) < r < 1.2r_l(a)$ the values obtained from the two expansions agree, typically, to about 1 part in 10^5. In this range the value of g_l is determined by linearly mixing the small- and large-r expansion values. Values for $f^{(n)}$ are determined from $f^{(n-1)}$ numerically using a five-point interpolation formula.[90]

Alternatively, one can determine the g_l by numerical integration of Eq. (D2). With this approach special care must be exercised when $r-a$ is small, i.e., where the slope of g_l is discontinuous. The difficulty is manifested by the peak in g_l at $r=a$ becoming increasingly sharp with increasing accuracy of the numerical integration.

Of course, neighboring atoms are generally not oriented in the z direction. The spherical harmonic expansion in Eq. (D1) must be appropriately transformed. The transformation of spherical harmonic expansions due to coordinate system rotation is discussed in Appendix E.

APPENDIX E: SYMMETRY

If the crystal structure is constrained to a particular space-group symmetry, then the amount of numerical labor can be considerably reduced by using the symmetry. Specifically, the charge density and potential for only one atom, called the ith atom, in a set of equivalent atoms, need be determined. The charge densities and potentials for all other atoms in that set can be determined from results for the ith atom.

Now let us consider the effect of point operations on atomic functions. Let the function $f(\mathbf{r})$ be expanded in terms of spherical harmonics about the ith atom,

$$f(\mathbf{r}) = \sum_{lm} f_{lm}(r_i) Y_{lm}(\hat{\mathbf{r}}_i). \tag{E1}$$

The rotation of a spherical harmonic is given by

$$RY_{lm}(\hat{\mathbf{r}}_i) = \sum_{m'} Y_{lm'}(\hat{\mathbf{r}}_i) D^{(l)}_{m'm}(R), \tag{E2}$$

where[91]

$$D^{(l)}_{m'm}(R) = \exp(-im'\alpha)\exp(-im\gamma)\sum_k \frac{(-1)^k[(l+m)!\,(l-m)!\,(l+m')!\,(l-m')!]^{1/2}}{k!\,(l+m-k)!\,(l-m'-k)!\,(k+m'-m)!}\left(\cos\frac{1}{2}\beta\right)^{2l-2k-m'+m}\left(-\sin\frac{1}{2}\beta\right)^{2k+m'-m} \tag{E3}$$

and α, β, γ are the Euler angles associated with the rotation R. Rotating the function f, we obtain

$$Rf(\mathbf{r}) = \sum_{lm} f^R_{lm}(r_i) Y_{lm}(\hat{\mathbf{r}}_i), \tag{E4}$$

where

$$f^R_{lm}(r_i) = \sum_{m'} D^{(l)}_{mm'}(R) f_{lm'}(r_i). \tag{E5}$$

We construct a symmetrization operator as

$$S^{(l)}_{imm'} = \frac{1}{|P_i|}\sum_j D^{(l)}_{mm'}(R_j), \tag{E6}$$

where the sum is over all elements of the point group P_i of the ith atom, R_j is the point operator part of the jth element

of P_i, and $|P_i|$ is the number of elements in P_i. The function $f^S(\mathbf{r})$ is "symmetrized," i.e., it has the symmetry of P_i,

$$f^S(\mathbf{r}) = \sum_{lm} f^S_{lm}(r_i) Y_{lm}(\hat{\mathbf{r}}_i), \tag{E7}$$

where

$$f^R_{lm}(r_i) = \sum_{m'} D^{(l)}_{mm'}(R) f_{lm'}(r_i). \tag{E8}$$

This symmetrization operator can be very useful. Suppose, for example, that there is a set of n equivalent neighbors to atom i. Let atom j be one of those neighbors in that set. Let us write that contribution of atom j to the potential energy of electrons in atom i as

$$V_{ij}(\mathbf{r}) = \sum_{lm} V_{ijlm}(r_i) Y_{lm}(\hat{\mathbf{r}}_i). \tag{E9}$$

The net contribution from every atom in that set is given by

$$V_i(\mathbf{r}) = \sum_j V_{ij}(\mathbf{r}) = \sum_{lm} V_{ilm}(r_i) Y_{lm}(\hat{\mathbf{r}}_i), \tag{E10}$$

where

$$V_{ilm}(r_i) = \sum_j V_{ijlm}(r_i). \tag{E11}$$

This same result can be obtained by

$$V_{ilm}(r_i) = n \sum_{m'} S_{imm'}^{(l)} V_{ijlm'}(r_i). \tag{E12}$$

Note that Eq. (E11) only requires the potential energy from one of the neighbors in the set and thus has an advantage over Eq. (E12). Computations need only be done for one atom from each set of equivalent neighbors.

---

*Corresponding author; michael.mehl@nrl.navy.mil

[1] M. Born and K. Huang, *Dynamical Theory of Crystal Lattices* (Oxford, London, 1954).

[2] R. G. Gordon and Y. S. Kim, J. Chem. Phys. **56**, 3122 (1972).

[3] P. Hohenberg and W. Kohn, Phys. Rev. **136**, B864 (1964).

[4] W. Kohn and L. J. Sham, Phys. Rev. **140**, A1133 (1965).

[5] J. F. Janak, V. L. Moruzzi, and A. R. Williams, Phys. Rev. B **12**, 1257 (1975).

[6] W. E. Rudge, Phys. Rev. **181**, 1033 (1969).

[7] B. Y. Tong, Phys. Rev. B **6**, 1189 (1972).

[8] F. W. Averill, Phys. Rev. B **6**, 3637 (1972).

[9] S. B. Trickey, F. R. Green, Jr., and F. W. Averill, Phys. Rev. B **8**, 4822 (1973).

[10] E. C. Snow, Phys. Rev. B **8**, 5391 (1973).

[11] M. J. Mehl, L. L. Boyer, and H. T. Stokes, J. Phys. Chem. Solids **57**, 1405 (1996).

[12] A. E. Mattsson, Science **298**, 759 (2002).

[13] P. Cortona, Phys. Rev. B **44**, 8454 (1991).

[14] A. Elci, Phys. Rev. B **46**, 2208 (1992).

[15] C. Muhlhausen and R. G. Gordon, Phys. Rev. B **23**, 900 (1981).

[16] R. LeSar, Phys. Rev. Lett. **61**, 2121 (1988).

[17] G. H. Wolf and M. S. T. Bukowinski, Phys. Chem. Miner. **15**, 209 (1988); H. Zhang and M. S. T. Bukowinski, Phys. Rev. B **44**, 2495 (1991).

[18] P. J. Edwardson, Phys. Rev. Lett. **63**, 55 (1989).

[19] E. Francisco, J. M. Recio, M. A. Blanco, A. M. Pendas, and L. Pueyo, Phys. Rev. B **51**, 2703 (1995).

[20] D. J. Lacks and R. G. Gordon, Phys. Rev. B **48**, 2889 (1993).

[21] M. J. Mehl, R. J. Hemley, and L. L. Boyer, Phys. Rev. B **33**, 8685 (1986); R. E. Cohen, Geophys. Res. Lett. **14**, 37 (1987).

[22] L. L. Boyer, M. J. Mehl, J. W. Flocken, and J. R. Hardy, Jpn. J. Appl. Phys., Suppl. **24**, 204 (1985).

[23] O. V. Ivanov and E. G. Maksimov, Phys. Rev. Lett. **69**, 108 (1992); Solid State Commun. **97**, 163 (1996).

[24] L. L. Boyer, R. E. Cohen, H. Krakauer, and W. A. Smith, Ferroelectrics **111**, 1 (1990).

[25] L. L. Boyer and M. J. Mehl, Ferroelectrics **150**, 13 (1993).

[26] L. L. Boyer, M. J. Mehl, and M. R. Pederson, Ferroelectrics **153**, 7 (1994).

[27] L. L. Boyer, H. T. Stokes, and M. J. Mehl, Ferroelectrics **164**, 177 (1995).

[28] H. T. Stokes, L. L. Boyer, and M. J. Mehl, Phys. Rev. B **54**, 7729 (1996).

[29] P. D. Tepesch, A. F. Kohan, E. D. Garbulsky, G. Ceder, C. Co-ley, H. T. Stokes, L. L. Boyer, M. J. Mehl, B. P. Burton, K. Cho, and J. Joannopoulos, J. Am. Ceram. Soc. **79**, 2033 (1996).

[30] L. L. Boyer, H. T. Stokes, and M. J. Mehl, Proceedings of the Fourth Williamsburg Workshop on First Principles Calculations for Ferroelectrics, edited by R. E. Cohen (Williamsburg, Virginia, 1996); L. L. Boyer, H. T. Stokes, and M. J. Mehl, Ferroelectrics **194**, 173 (1997).

[31] N. Marzari and D. Vanderbilt, in *First Principles Calculations for Ferroelectrics*, AIP Conference Proceedings No. 436, edited by R. E. Cohen (AIP, New York, 1998), p. 146.

[32] N. Marzari and D. Vanderbilt, Phys. Rev. B **56**, 12847 (1997).

[33] L. L. Boyer, H. T. Stokes, and M. J. Mehl, in *First Principles Calculations for Ferroelectrics*, AIP Conference Proceedings No. 436, edited by R. E. Cohen (AIP, New York, 1998), p. 227.

[34] L. L. Boyer, H. T. Stokes, and M. J. Mehl, Phys. Rev. Lett. **84**, 709 (2000).

[35] W. N. Mei, L. L. Boyer, M. J. Mehl, M. M. Ossowski, and H. T. Stokes, Phys. Rev. B **61**, 11425 (2000).

[36] H. T. Stokes, C. Sadate, D. M. Hatch, L. L. Boyer, and M. J. Mehl, Phys. Rev. B **65**, 064105 (2002).

[37] M. M. Ossowski, L. L. Boyer, M. J. Mehl, and H. T. Stokes, Phys. Rev. B **66**, 224302 (2002).

[38] R. Resta, Rev. Mod. Phys. **66**, 899 (1994).

[39] L. L. Boyer, M. J. Mehl, and H. T. Stokes, Phys. Rev. B **66**, 092106 (2002).

[40] M. M. Ossowski, L. L. Boyer, M. J. Mehl, and M. R. Pederson, Phys. Rev. B **68**, 245107 (2003).

[41] L. L. Boyer, M. J. Mehl, and D. Finkenstadt, Phys. Rev. B **75**, 132103 (2007).

[42] J. F. Janak, Phys. Rev. B **18**, 7165 (1978).

[43] E. Clementi and C. Roetti, At. Data Nucl. Data Tables **14**, 177 (1974).

[44] A. D. McLean and R. S. McLean, At. Data Nucl. Data Tables **26**, 197 (1981).

[45] A. R. Edmonds, *Angular Momentum in Quantum Mechanics* (Princeton University, Princeton, 1960).

[46] L. Barnes, Ph.D. thesis, Brigham Young University, 2000.

[47] H. Hellman, *Einführung in die Quanten Theorie* (Deuticke, Leipzig, 1937), p. 285.

[48] R. P. Feynman, Phys. Rev. **56**, 340 (1939).

[49] P. Pulay, in *Modern Theoretical Chemistry*, edited by H. F. Schaeffer III (Plenum, New York, 1977).

[50] P. Pulay, Mol. Phys. **17**, 197 (1969).

[51] M. R. Pederson and K. A. Jackson, Phys. Rev. B **41**, 7453

(1990).

[52] K. A. Jackson and M. R. Pederson, Phys. Rev. B **42**, 3276 (1990).

[53] M. R. Pederson and K. A. Jackson, Phys. Rev. B **43**, 7312 (1991).

[54] A. A. Quong, M. R. Pederson, and J. L. Feldman, Solid State Commun. **87**, 535 (1993).

[55] D. V. Porezag and M. R. Pederson, Phys. Rev. B **54**, 7830 (1996).

[56] D. V. Porezag, Ph.D. thesis, Technische Universitait, 1997.

[57] A. Briley, M. R. Pederson, K. A. Jackson, D. C. Patton, and D. V. Porezag, Phys. Rev. B **58**, 1786 (1998).

[58] J. P. Perdew and Y. Wang Phys. Rev. B **45**, 13244 (1992).

[59] D. V. Porezag and M. R. Pederson, Phys. Rev. A **60**, 2840 (1999).

[60] H. T. Stokes and L. L. Boyer (stokes.byu.edu/isotropy.html.).

[61] H. T. Stokes and D. M. Hatch, *Isotropy Subgroups of the 230 Crystallographic Space Groups* (World Scientific, Singapore, 1988).

[62] W. Cochran and R. A. Cowley, J. Phys. Chem. Solids **23**, 447 (1962).

[63] P. Giannozzi, S. de Gironcoli, P. Pavone, and S. Baroni, Phys. Rev. B **43**, 7231 (1991).

[64] Ph. Daniel, A. Bulou, M. Rousseau, J. Nouet, J. L. Fourquet, M. Leblanc, and R. Burriel, J. Phys.: Condens. Matter **2**, 5663 (1990).

[65] V. I. Zinenko and N. G. Zamkova, Phys. Solid State **42**, 1348 (2000).

[66] S. C. Miller and W. F. Love, *Tables of Irreducible Representations Space Groups and Co-Representations of Magnetic Space Groups* (Pruett, Boulder, 1967).

[67] Y. R. Chen, V. Perebeinos, and P. B. Allen, Phys. Rev. B **69**, 054109 (2004).

[68] O. K. Andersen, Phys. Rev. B **12**, 3060 (1975).

[69] S.-H. Wei and H. Krakauer, Phys. Rev. Lett. **55**, 1200 (1985).

[70] D. Singh, Phys. Rev. B **43**, 6388 (1991).

[71] B. N. Harmon, D. D. Koelling, and A. J. Freeman, J. Phys. C **6**, 2294 (1973).

[72] L. Hedin and B. I. Lundqvist, J. Phys. C **4**, 2064 (1971).

[73] F. Birch, J. Geophys. Res. **83**, 1257 (1978).

[74] C.-Z. Wang, R. Yu, and H. Krakauer, Phys. Rev. B **53**, 5430 (1996).

[75] E. Wigner, Phys. Rev. **46**, 1002 (1934).

[76] K. Karch, P. Pavone, W. Windl, O. Schütt, and D. Strauch, Phys. Rev. B **50**, 17054 (1994).

[77] D. W. Feldman, James H. Parker, Jr., W. J. Choyke, and Lyle Patrick, Phys. Rev. **173**, 787 (1968).

[78] N. Bernstein, H. J. Gotsis, D. A. Papaconstantopoulos, and M. J. Mehl, Phys. Rev. B **71**, 075203 (2005).

[79] R. E. Cohen, Nature (London) **358**, 136 (1992).

[80] D. J. Singh, Ferroelectrics **164**, 143 (1995).

[81] Z. Wu, R. E. Cohen, and D. J. Singh, Phys. Rev. B **70**, 104112 (2004).

[82] C. S. Hellberg, W. E. Pickett, L. L. Boyer, H. T. Stokes, and M. J. Mehl, J. Phys. Soc. Jpn. **68**, 3489 (1999).

[83] D. L. Lacks and R. G. Gordon, J. Chem. Phys. **100**, 4446 (1994).

[84] L. H. Thomas, Proc. Cambridge Philos. Soc. **23**, 542 (1926).

[85] E. Fermi, Z. Phys. **48**, 73 (1928).

[86] C. F. von Weizsácker, Z. Phys. **96**, 431 (1935).

[87] J. C. Slater, *Insulators, Semiconductors and Metals: Quantum Theory of Molecules and Solids* (McGraw-Hill, New York, 1967), Vol. 3, Appendix 4.

[88] G. C. Fletcher, *The Electron Band Theory of Solids* (North-Holland, Amsterdam, 1971), p. 213.

[89] *Mathematica 5.0* (Wolfram Research Inc., Champaign, IL, 2003).

[90] *Handbook of Mathematical Functions*, edited by M. Abramowitz and I. Stegun (Dover, New York, 1970), Eq. 25.3.6.

[91] M. Tinkham, *Group Theory and Quantum Mechanics* (McGraw-Hill, New York, 1964).